Mechanism of Ice-Band Pattern Formation Caused by Resonant Interaction between Sea Ice and Internal Waves in a Continuously Stratified Ocean

RYU SAIKI*†, HUMIO MITSUDERA†, AYUMI FUJISAKI-MANOME‡, NORIAKI KIMURA*,

JINRO UKITA§, TAKENOBU TOYOTA† AND TOMOHIRO NAKAMURA†

* *Atmosphere and Ocean Reserch Institute, the University of Tokyo, Kashiwa, Japan.*

† *Institute of Low Temperature Science, Hokkaido University, Sapporo, Japan*

‡ *Cooperative Institute for Great Lake Research (CIGLR), University of Michigan, Climate and Space Science and Engineering, Ann Arbor, MI*

§ *Faculty of Science Niigata University, Niigata, Japan*

ABSTRACT

In polar oceans, ice-band patterns are frequently observed around the ice edge in the winter, where sea ice production and melting continually occur. A better understanding of such fundamental processes in marginal ice zones (MIZs) may be key to accurate predictions of sea-ice evolution. Ice bands exhibit approximately 10-km-scale regular band spacings, and their long axes turn to the counter-clockwise (clockwise) with respect to the wind direction in the Northern (Southern) Hemisphere. We formulate a theory that is relevant for a continuously stratified ocean and compare the theoretical results with the numerical-model results and satellite observations. The numerical results quantitatively agree well with the theory. In particular, resonance condition, on which the phase speed of internal wave matches with the ice-band propagation speed, is always satisfied even if wind speed becomes slow. This is because there are an infinite number of baroclinic modes in continuously stratified ocean. We also show that an ice-band pattern emerges from a random initial ice concentration even though the wind is homogeneous. Plume-like ice bands along ice edge, which are frequently observed by satellites, are well explained by the pattern formation from random noise. Various effects of the ice-band formation were

explored with respect to the relationship between the initial ice concentration and the wind direction, ice roughness, ice thickness, temporal variation of wind, and the Coriolis parameter.

1 Introduction

Sea-ice production and melting considerably affect global climate by modifying heat, salt, and freshwater distributions (*Broecker*, 2010; *Rudels et al.*, 2015; *Rudels*, 2016). Marginal ice zones (MIZs) that lie adjacent to open water are characterized by vigorous interactions among ocean and atmosphere through sea ice (*Wadhams*, 2000). In light of rapid decreasing sea ice trend in the Arctic Ocean and highly contrasting signals observed in the Southern Ocean (e.g., *Stroeve et al.*, 2012; *Gascard et al*, 2019; *Parkinson et al.*, 2019), it is important to understand physical processes in the MIZ.

MIZs exist between open ocean and interior ice pack. In MIZ, the size of floes is usually less than 100 m, exhibiting fractal size distribution (*Toyota et al.*, 2006; *Toyota et al.*, 2016). The melting rate is sensitive to the floe size; small floes with a size < 30 m are easily melted by heat from the upper ocean (*Steele*, 1992). The sea surface temperature in MIZs is significantly influenced by the submesoscale fronts and eddies (e.g. *Swart et al.*, 2020; *Manucharian and Thompson*, 2017), as well as by the internal waves, which cause the downward flux of momentum and energy, resulting in turbulent mixing in the upper ocean (e.g., *McPhee and Kantha*, 1989). Recently, *Kawaguchi et al.* (2016)

reported that subsurface mixing is further enhanced by the breaking of submesoscale internal inertia-gravity waves trapped in an anticyclonic eddy around the ice edge area in the Chukchi Plateau. Therefore, understanding the submesoscale ice-ocean interaction in MIZs is key for the better the evolution of sea ice extent.

One characteristic of the submesoscale phenomena in MIZs is ice bands. For example, Figs. 1b, d are the visible satellite images showing plume-like ice bands adjacent to the offshore ice edge in the East Greenland Current and Arctic Sea, retrieved by the Moderate-Resolution Imaging Spectroradiometer (MODIS) with 250 m resolution, in which winds analyzed by the European Center for Medium-range Weather Forecasts (ECMWF) are also superimposed. The ice bands typically have a regular spacing of 10-km-scale. Plume-like ice bands such as those shown in Fig. 1b can be observed throughout the winter season in the East Greenland Current. Similar ice-band formation has been observed in the Bering Sea (*Muench and Charnel*, 1977), the Sea of Okhotsk (*Saiki and Mitsudera*, 2016), and the Southern Ocean (*Ishida and Ohshima*, 2009).

Ice bands are of various lengths ranging from 1 km to 10 km. For example, *McPhee* (1979, 1982, 1983) observed ice bands of several hundred meters to 1-km-scale during ship observations. They suggested that an ice band is formed by the ice-edge speed acceleration caused by ice melting and enhanced stratification at a MIZ, which separates an ice band from the sea-ice area. *Wadhams* (1983) indicated that the 1-km-scale ice bands are generated by the radiation stress due to fetch-limited surface waves that gather ice floes. *Muench and Charnel* (1977) and *Ishida and Ohshima* (2009) observed ice bands with a spacing of 10-km-scale from satellite infra-red images. *Muench et al.* (1983) and *Fujisaki and Oey* (2011) suggested that ice bands may be generated by the internal lee waves from an ice edge. *Ishida and Ohshima* (2009) described the characteristics of this type of submesoscale ice bands as follows: (1) ice bands have a regular band spacing of approximately 10 km, and they become wider as the wind becomes stronger; and (2) the long axis of an ice band turns to the counter-clockwise (clockwise) with respect to the predominant wind direction in the Northern (Southern) Hemisphere.

Saiki and Mitsudera (2016) explained these basic characters from the viewpoint of resonant interaction in the ice–ocean coupled system. They used a reduced gravity, 1.5-layer ocean model, coupled with a simple ice drifting model, and discussed a linear instability problem in this system. They showed that when an off-ice wind blows, ice moves in the off-ice direction, which accelerates an upper-ocean flow because the ice-water stress is larger than the air-water stress. Since the acceleration of the upper-ocean flow is the largest at the center of an ice band, where the ice concentration is largest, the upper-layer flow converges and downwelling occurs at the ice band (see Fig. 4 of *Saiki and Mitsudera*, 2016). This downwelling forces the density interface, and generates an internal inertia-gravity wave. On the other hand, the interfacial motion associated with the internal inertia-gravity wave causes convergence/divergence in the upper-layer velocity, which increase/decrease the ice concentration, resulting in the formation of the ice-band structure. An ice band grows when the upper-ocean velocity associated with ice-water stress and the velocity associated with the internal inertia-gravity wave cause positive feedback (see Fig. 8 of *Saiki and Mitsudera*, 2016). Submesoscale internal waves generated by the above ice-ocean coupled system may enhance turbulent mixing and affect the thermal conditions in the upper ocean (e.g., *McPhee and Kantha*, 1987; *Kawaguchi et al.*, 2016).

In the present study, we investigate ice-band formation in a continuously stratified ocean. We revisit the problem with a continuously stratified ocean model because the 1.5-layer model that *Saiki and Mitsudera* (2016) studied is too simple to apply directly.

One of differences between the two models is that the continuously stratified model has an infinite number of baroclinic modes, whereas the 1.5-layer model has only one baroclinic mode. This may modify the resonance condition between the sea ice and the internal waves. For example, internal inertia-gravity waves in the 1.5-layer model has a minimum phase speed, and therefore, there is a cut-off wind speed below which ice-band formation does not occur. In contrast, a continuously stratified model has no minimum phase speed because there are an infinite number of modes in which a higher mode wave has a slower phase speed, implying that there is no cut-off wind speed. As such, ice bands in reality will be better described by continuously stratified ocean models.

A major purpose of this study is to quantitatively compare the ice-band theory with numerical modeling results and satellite observations. Here, we present that the observations of the submesoscale band spacings of 10-km-scale agrees well with the theory and numerical results. Further, the numerical results exhibit the change in the most-unstable mode with wind speed changes, which is consistent with the theory. We also investigated the growth rate, focusing on the wind direction relative to the ice band pattern. If the ice-edge area includes initial random disturbances, like small ice floes in MIZs, the ice bands' growth depends on the most unstable mode even though the ice edge imposes a strong initial disturbance on the ice-ocean coupled system. We found that the pattern formation from random initial conditions explains the plume-like ice-band structure well. This structure is perpendicularly to the ice edge in MIZs as shown in Figs. 1b, d.

We further discuss various effects that control ice band formation, such as ice concentration, ice thickness, ice stresses, wind temporal change, and the effects of the Earth's rotation. Ice concentration may affect the band formation because ice movement will be restricted when the ice concentration is sufficiently high. Sea ice stresses also have significant effects because the bands form as a result of the surface stress difference between ice and water as seen in Fig. 4 of *Saiki and Mitsudera* (2016). Further, ice band formation was observed in a broad ice area in the Sea of Okhotsk when a low-pressure system passed an ice edge in early spring (*Saiki and Mitsudera*, 2016). Thus, we investigate whether the theory is applicable to the temporary change in wind with a synoptic timescale. Finally, the effects of the Earth's rotation are discussed because the ice bands are observed in a relatively broad latitudinal range from approximately 45 ° N in the Sea of Okhotsk to 80 ° N in the Arctic Sea. We aim to discuss the conditions of ice-band formation through these sensitivity experiments.

The remainder of this paper is organized as follows. In Section 2, we formulate a mechanism of ice-band pattern formation in a continuously stratified ocean. In Section 3, we reproduce ice-band pattern formation in a continuously stratified ocean using a numerical model and compare the numerical results with the theory. In Section 4, we validate the theory and numerical results from the satellite observations. The results of the sensitivity studies are presented in Section 5. Finally, we discuss and summarize the results in Section 6.

2 Theoretical considerations on ice-band pattern formation over continuously stratified ocean

Here, we formulate the basic equations of an ice-ocean coupled system with continuous stratification in the ocean over a flat bottom with depth D. The sea surface is covered by sea ice with concentration A, which is the ratio of sea-ice cover within an unit area and is represented from zero to one.

2.1 Surface stresses over the MIZ

The sea-ice drift is driven by a homogeneous wind. We consider an eigenvalue problem for an ice band, which gives the band width and turning angle of the band as those of an unstable mode with a maximum growth rate. Figure 2a shows the coordinate system and sea-ice motion. The x-direction is defined by the band pattern propagation direction, and the y-direction is perpendicular to it. Because we assume that variables are independent of y for the theoretical development, y represents the orientation of the long axis of the bands. $\boldsymbol{\tau}_{ai}, \boldsymbol{\tau}_{iw}$, and $\boldsymbol{\tau}_{aw}$ are the air–ice, ice–water, and air–water stresses, respectively. θ_a denotes the wind direction associated with both $\boldsymbol{\tau}_{ai}$ and $\boldsymbol{\tau}_{aw}$, while θ_i is the direction of $\boldsymbol{\tau}_{iw}$. $\delta\theta$ is the turning angle between $\boldsymbol{\tau}_{ai}$ and $\boldsymbol{\tau}_{iw}$, which occurs as a result of the Earth's rotation. The stress applied to the sea surface is then written as

$$\boldsymbol{\tau} \;=\; A\boldsymbol{\tau}_{iw} + (1-A)\boldsymbol{\tau}_{aw},$$

where A is the ice concentration (Fig. 2b). We consider that $\boldsymbol{\tau}$ depends solely on A; $\boldsymbol{\tau}_{iw}$, and $\boldsymbol{\tau}_{aw}$ represent sea ice characteristics such as ice roughness, which are assumed to be constants. Now, $\boldsymbol{\tau}$ is divided into the temporal mean and a perturbation such that $\boldsymbol{\tau} = \overline{\boldsymbol{\tau}} + \boldsymbol{\tau}'$, where the bar denotes the mean, and the prime denotes the perturbation. If we assume $\boldsymbol{\tau}_{iw}$ and $\boldsymbol{\tau}_{aw}$ are given, $\boldsymbol{\tau}'$ is written as $\boldsymbol{\tau}' = A'(\boldsymbol{\tau}_{iw} - \boldsymbol{\tau}_{aw})$, where A' is the perturbation in terms of the ice concentration, while $\overline{\boldsymbol{\tau}} = \overline{A}\boldsymbol{\tau}_{iw} + (1 - \overline{A})\boldsymbol{\tau}_{aw}$, where $\overline{A}$ denotes the mean. The specific form of $\boldsymbol{\tau}'$ yields (see Appendix 1 for the derivation)

$$\boldsymbol{\tau}' = A' \left(\frac{\delta\tau}{|\boldsymbol{\tau}_{ai}|} \boldsymbol{\tau}_{ai} - (\sin \delta\theta) \boldsymbol{k} \times \boldsymbol{\tau}_{ai} \right), \tag{1}$$

where $\delta\tau = |\boldsymbol{\tau}_{ai}| \cos \delta\theta - |\boldsymbol{\tau}_{aw}|$, and $\boldsymbol{k}$ denotes the unit vector in the vertical direction.

2.2 Internal inertia-gravity waves in the ocean

The governing equations for a continuously stratified ocean are written as follows:

$$\frac{\partial \boldsymbol{u}'}{\partial t} + f\boldsymbol{k} \times \boldsymbol{u}' = -\frac{1}{\rho_w}\frac{\partial p'}{\partial x}\boldsymbol{i} + \frac{1}{\rho_w}\frac{\partial \boldsymbol{\tau}'}{\partial z}, \tag{2}$$

$$\frac{\partial u'}{\partial x} + \frac{\partial w'}{\partial z} = 0, \tag{3}$$

$$\frac{\partial \rho'}{\partial t} - \frac{\rho_w N_B^2}{g} w' = 0, \tag{4}$$

$$\frac{\partial p'}{\partial z} = -\rho' g, \tag{5}$$

where $\boldsymbol{u}' = (u', v')$ and w' are velocity perturbations of the x, y, and z-components, respectively; p' is the pressure perturbation; and $\boldsymbol{i}$ is a unit vector of the x-component. Note that we assumed that the ice-band pattern is independent of y. ρ_w is the representative ocean density, $\overline{\rho}(z)$ is the vertical density profile of the background, ρ' is the density perturbation, f is the Coriolis parameter, g is the gravity acceleration, and N_B is the Brunt–Väisälä frequency $N_B^2 = -(g/\rho_w)(d\overline{\rho}/dz)$. Here, we set $w' = 0$ and $\rho' = 0$ at the sea surface ($z = 0$) and the bottom ($z = -D$) as the boundary conditions.

Next, we assume that the variables may be written using the vertical structure functions $\hat{p}_n(z), \hat{q}_n(z)$ as follows:

$$p'(x, y, z, t) = g\rho_w \sum_{n=1}^{\infty} \tilde{\eta}_n(x, y, t)\hat{p}_n(z), \tag{6}$$

$$\boldsymbol{u}'(x, y, z, t) = \sum_{n=1}^{\infty} \tilde{\boldsymbol{u}}_n(x, y, t)\hat{p}_n(z), \tag{7}$$

$$w'(x, y, z, t) = \sum_{n=1}^{\infty} \tilde{w}_n(x, y, t)\hat{q}_n(z), \tag{8}$$

$$\rho'(x, y, z, t) = \sum_{n=1}^{\infty} \tilde{\rho}_n(x, y, t)\hat{q}_n(z), \tag{9}$$

where

$$\frac{d}{dz}\left(\frac{1}{N_B^2}\frac{d\hat{p}_n}{dz}\right)+\frac{\hat{p}_n}{\hat{c}_n^2}=0,\ \frac{d}{dz}\left(\frac{1}{N_B^2}\frac{d\hat{q}_n}{dz}\right)+\frac{\hat{q}_n}{\hat{c}_n^2}=0, \tag{10}$$

$$\frac{d\hat{p}_n}{dz}=0,\ \hat{q}_n=0 \qquad \text{at} \qquad z=0,-D, \tag{11}$$

where n (=1,2,3, $\cdots$) denotes a mode number, and $\hat{c}_n$ is the eigenvalue of the n-th baroclinic mode. The orthogonality and normalization condition is $\int_{-D}^{0}\hat{p}_n\hat{p}_m dz = I_n\delta_{nm}$, where δ_{nm} is Kronecker's delta. We impose $I_n = D$ to let $\hat{p}$ be a nondimensional structure function. Here, we refer to $\hat{c_n}$ as the baroclinic phase speed, which represents the nondispersive limit of the phase speed of internal inertia-gravity waves. Further, we assume a forcing function

$$\frac{\partial \boldsymbol{\tau}'}{\partial z}=\left(\frac{\partial \tau^x}{\partial z},\frac{\partial \tau^y}{\partial z}\right)=\begin{cases}\left(\frac{\tau^x}{h_E},\frac{\tau^y}{h_E}\right) & -h_E < z \le 0,\\ 0 & -D < z \le -h_E,\end{cases} \tag{12}$$

where h_E is a forcing depth corresponding to the Ekman layer thickness (e.g., *Fujisaki and Oey*, 2011). Then, the momentum equations become

$$\frac{\partial \tilde{u}_n}{\partial t} - f\tilde{v}_n + g\frac{\partial \tilde{\eta}_n}{\partial x} = \tilde{\tau}_n{}^x, \tag{13a}$$

$$\frac{\partial \tilde{v}_n}{\partial t} + f\tilde{u}_n = \tilde{\tau}_n{}^y, \tag{13b}$$

$$\text{where} \qquad \tilde{\boldsymbol{\tau}}_n = \frac{b_n}{\rho_w}\frac{\boldsymbol{\tau}'}{h_E}, \tag{13c}$$

$$\text{and} \qquad b_n = \frac{1}{D}\int_{-h_E}^{0} \hat{p}_n dz. \tag{13d}$$

Further, using (4) and (5), the equation of continuity (3) is rewritten as

$$\frac{\hat{c}_n{}^2}{g}\frac{\partial \tilde{u}_n}{\partial x} + \frac{\partial \tilde{\eta}_n}{\partial t} = 0. \tag{14}$$

Thus, the basic equations may be written in terms of $\tilde{\eta}_n$ using (1), (12), (13), (14), (A1) and (A2) as follows:

$$\begin{aligned} &\tfrac{\partial}{\partial t}\left[\left(\tfrac{\partial^2}{\partial t^2} + f^2\right)\tilde{\eta}_n - \hat{c}_n^2\tfrac{\partial^2 \tilde{\eta}_n}{\partial x^2}\right] \\ &= -h_n\left[\tfrac{\partial^2 A'}{\partial t \partial x}\left(\delta_d{}^* \ \tilde{\tau}_{ai}{}^{x}{}_{n} + \tilde{\tau}_{ai}{}^{y}{}_{n}\sin\delta\theta\right) + f\tfrac{\partial A'}{\partial x}\left(\delta_d{}^* \ \tilde{\tau}_{ai}{}^{y}{}_{n} - \tilde{\tau}_{ai}{}^{x}{}_{n}\sin\delta\theta\right)\right], \end{aligned} \tag{15}$$

where $\delta_d^* = (|\boldsymbol{\tau}_{\boldsymbol{ai}}| \cos\delta\theta - |\boldsymbol{\tau}_{aw}|)/|\boldsymbol{\tau}_{ai}|$ represents the nondimensional stress difference between the ice-covered ocean and the open ocean, $\delta\theta = \theta_a - \theta_i$ denotes the turning angle between air–ice and ice–ocean stresses, and $h_n = \frac{\hat{c}_n^2}{g}$.

2.3 Evolution of sea ice concentration

The linear evolution equation for the sea-ice concentration at the sea surface ($z = 0$) is evaluated by the continuity of ice concentration, which is written as follows:

$$\frac{\partial A'}{\partial t} + \overline{U}_i \frac{\partial A'}{\partial x} + \overline{A} \sum_{m=1}^{\infty} \frac{\partial \tilde{u}_m}{\partial x} \hat{p}_m(0) = 0, \tag{16}$$

where we recall that $\overline{U}_i$ is defined as the band pattern propagation speed (see Fig. 2a). Therefore, equation (16) is rewritten using (14) as follows:

$$\frac{\partial A'}{\partial t} + \overline{U}_i \frac{\partial A'}{\partial x} - \sum_{m=1}^{\infty} \frac{\overline{A}}{h_m} \frac{\partial \tilde{\eta}_m}{\partial t} \hat{p}_m(0) = 0. \tag{17}$$

The internal wave equation (15) and the equation of the sea-ice concentration development (17) in the continuous stratification are thus derived.

2.4 Scaling

Next, we discuss how the band spacing and turning angle are determined in an ocean with continuous stratification. First, (15) and (17) are nondimensionalized as follows:

$$t = f^{-1}t^*, \quad x = Lx^*, \quad z = Dz^*, \quad h_E = Dh_E^*, \quad \tilde{\eta}_n = \frac{f^2L^2}{g}\tilde{\eta}_n{}^*,$$

$$(\tilde{u}_n, \tilde{v}_n) = fL(\tilde{u}_n{}^*, \tilde{v}_n{}^*), \quad \overline{U}_i = fL\overline{U}_i{}^*, \quad gh_n = \hat{c}_n^2 = (fL\hat{c}_n{}^*)^2,$$

$$\boldsymbol{\tau}_{ai} = \epsilon\rho_w f^2 LD\boldsymbol{\tau}_{ai}{}^*, \text{ and } \boldsymbol{\tau}' = \epsilon\rho_w f^2 LD\boldsymbol{\tau}'^*,$$

where we define $\epsilon = h_E/D$, which is equivalent to a scaled Ekman layer depth. Here, the asterisk(*) denotes a non-dimensional quantity, and L and D are typical values of the horizontal and vertical scale, respectively. Thus, the forcing function $\tilde{\boldsymbol{\tau}}_n$ in (13a, b) is nondimensionalized as

$$\tilde{\boldsymbol{\tau}}_n = \frac{\boldsymbol{\tau}'}{\rho_w h_E} b_n = \epsilon f^2 L \frac{\boldsymbol{\tau}'^* b_n}{h_E^*}.$$

We define

$$\tilde{\boldsymbol{\tau}}_n{}^* = \frac{\boldsymbol{\tau}'^* b_n}{h_E^*} \quad \text{and} \quad \tilde{\boldsymbol{\tau}}_{ai}{}^*{}_n = \frac{\boldsymbol{\tau}_{ai}'^* b_n}{h_E^*},$$

and obtain a scaling of the stress such that

$$\tilde{\boldsymbol{\tau}}_n = \epsilon f^2 L \tilde{\boldsymbol{\tau}}_n{}^* \quad \text{and} \quad \tilde{\boldsymbol{\tau}}_{ai\ n} = \epsilon f^2 L \tilde{\boldsymbol{\tau}}_{ai}{}^*{}_n.$$

Note that $\tilde{\boldsymbol{\tau}}_n{}^*$ and $\tilde{\boldsymbol{\tau}}_{ai}{}^*{}_n$ are $O(1)$ because, from (13d),

$$b_n = \frac{1}{D}\int_{-h_E}^{0} \hat{p}_n dz = \int_{-h_E^*}^{0} \hat{p}_n dz^* = O(h_E^*).$$

By substituting a plane wave solution with respect to $\tilde{\eta}_n$ and A', we have derived a characteristic equation (A6) in Appendix 2.

2.5 Ice bands in a continuously stratified ocean

Resonance occurs when the propagation speed of the ice-band pattern coincides with the phase speed of the internal inertia-gravity wave. Each mode has one resonance point (at most) (see, e.g., Fig 3a). A resonance condition yields (see Equation (A6) in Appendix 2)

$$\begin{aligned}&[\omega^{*2} - (1 + \hat{c}_n^{*2} k^{*2})]\,(\omega^* - \overline{U}_i^{\,*} k^*)\\ &-\epsilon\overline{A}\hat{p}_n(0)\,[i\omega^* k*(\delta_d^{\,*}\tilde{\tau}_{ai\ n}^{\ x*} + (\sin\delta\theta)\tilde{\tau}_{ai\ n}^{\ y*}) - k^*(\delta_d^{\,*}\tilde{\tau}_{ai\ n}^{\ y*} - (\sin\delta\theta)\tilde{\tau}_{ai\ n}^{\ x*})] = 0,\end{aligned} \tag{18}$$

for the n-th mode, where ω^* is a non-dimensional frequency, and k^* is a non-dimensional wave number. Recall that $\delta_d^{\,*} = \Delta\tilde{\tau}/|\boldsymbol{\tau}_{ai}|$, and $\delta\theta$ is the turning angle between $\boldsymbol{\tau}_{ai}$ and $\boldsymbol{\tau}_{iw}$.

2.5.1 Band spacing

Considering that ϵ, which is equivalent to the scaled Ekman depth, is a small parameter, we conduct a perturbation expansion of (18) in terms of ϵ in the vicinity of the resonance point $(\omega_{0n}^*, k_{0n}^*)$, where $k_n^* = k_{0n}^* + \epsilon^{\frac{1}{2}} k_{1n}^* + \cdots$, and $\omega_n^* = \omega_{0n}^* + \epsilon^{\frac{1}{2}}\omega_{1n}^* + \cdots$. The resonance point (ω_{0n}^*, k_{0n}^*) can be obtained by the leading order ($O(\epsilon^0)$) of (18) as follows:

$$\omega_{0n}^{*2} - (1 + \hat{c}_n{}^{*2} k_{0n}{}^{*2}) = 0, \tag{19}$$

$$\omega_{0n}^* - \overline{U}_i{}^* k_{0n}^* = 0. \tag{20}$$

Equation (19) denotes a non-dimensional dispersion relationship of the internal inertia gravity wave, while (20) represents the band pattern propagation speed. Therefore, k_{0n}^* at the intersection in the $k^* - \omega^*$ plane (e.g., Fig. 3a) determines the band spacing $\lambda_n{}^*$ such that

$$\lambda_n{}^* = \frac{2\pi}{k_{0n}^*} = 2\pi \left(\overline{U}_i{}^{*2} - \hat{c}_n{}^{*2} \right)^{\frac{1}{2}}. \tag{21}$$

Figure 3a shows the dispersion relationship of the lowest three modes of the internal inertia-gravity waves in the continuous stratification of Fig. 4. The intersection $(k_{0n}^*, \omega_{0n}^*)$ occurs for each mode as long as $\overline{U}_i{}^* > \hat{c}_n{}^*$ (see (21)). This implies that lower modes, which have a larger $\hat{c}_n{}^*$, would not be resonant when $\overline{U}_i{}^* < \hat{c}_n{}^*$. In contrast, among the possible resonant modes, the band spacing becomes wider if the resonance occurs due to the higher-mode internal wave.

2.5.2 Growth rate and wind direction

Next, the growth rate of the ice-band pattern development is derived from the $O(\epsilon)$ perturbation of (18). Thus, we obtain

$$\begin{aligned}\omega_{1n}^{*} &= \pm\left(\overline{A}\hat{p}_n(0)\frac{k_{0n}^{*}G}{2}\right)^{\frac{1}{2}} e^{i\frac{\phi}{2}} + \hat{c}_n{}^{*}k_{1n}^{*} \\ &= \pm\left(\overline{A}\hat{p}_n(0)\frac{k_{0n}^{*}G}{2}\right)^{\frac{1}{2}} (\cos\tfrac{\phi}{2} + i\sin\tfrac{\phi}{2}) + \hat{c}_n{}^{*}k_{1n},\end{aligned} \tag{22}$$

where

$$G = [(1/\omega_{0n}^{*2})(\delta_d{}^{*}\tilde{\tau}_{ai}{}^{y*} - (\sin\delta\theta)\tilde{\tau}_{ai}{}^{x*})^2 + (\delta_d{}^{*}\tilde{\tau}_{ai}{}^{x*} + (\sin\delta\theta)\tilde{\tau}_{ai}{}^{y*})^2]^{\frac{1}{2}},$$

$$\tan\phi = \frac{\delta_d{}^{*}\tilde{\tau}_{ai}{}^{x*} + \sin\delta\theta\tilde{\tau}_{ai}{}^{y*}}{(\sin\delta\theta)\tilde{\tau}_{ai}{}^{x*} - \delta_d{}^{*}\tilde{\tau}_{ai}{}^{y*}}\omega_{0n}^{*} = \frac{\delta_d{}^{*} + \sin\delta\theta\tan\theta_a}{(\sin\delta\theta) - \delta_d{}^{*}\tan\theta_a}\omega_{0n}^{*},$$

where ϕ is defined for $-\pi/2 < \phi < \pi/2$. The growth rate of ice band $\nu_n{}^{*}$ is the imaginary part of ω_{1n}^{*}, and it is a function of the turning angle θ_a, as in Fig. 5. The maximum growth rate is obtained when

$$\frac{\tilde{\tau}_{ai}^{y*}}{\tilde{\tau}_{ai}^{x*}} = \tan\theta_a = \frac{\sin\delta\theta}{\delta_d^{\ *}}, \tag{23}$$

where $\delta\theta$ denotes the angle between $\boldsymbol{\tau}_{iw}$ and $\boldsymbol{\tau}_{ai}$, and $\delta_d^{\ *}$ represents the stress difference between the air–water interface and air–ice interface. Equation (23) indicates that the maximum growth occurs if the wind direction turns to the counter-clockwise (when $\tan\theta_a > 0$) with respect to the propagation direction of the ice band. If the wind direction turns to the clockwise (when $\tan\theta_a < 0$) with respect to the propagation direction of the ice band, the growth rate of the ice band reduces as shown in Fig. 5.

2.5.3 Modes of the maximum growth

The maximum growth rate for each mode ${\nu_n}^*_{max}$ may be derived by substituting (23) into (22) as follows:

$${\nu_n}^*_{max} = \frac{k_{0n}^*|\tilde{\boldsymbol{\tau}}_{ai\ n}^{\ *}|^{\frac{1}{2}}({\delta_d}^{*2} + \sin^2\delta\theta)^{\frac{1}{4}}}{2}. \tag{24}$$

This implies that the nondimensional maximum growth rate ${\nu_n}^*_{max}$ is proportional to the wave number k^*_{0n}. Therefore, for a given ${\overline{U}_i}^*$, the growth rate is higher if the mode number is lower, because the wave number k^*_{0n} at the resonance point is larger for the lower mode. We also consider ${\tilde{\boldsymbol{\tau}}_{ai}}^*{}_n$ in (24). If we assume that N_B is constant, then ${\tilde{\boldsymbol{\tau}}_{ai}}^*{}_n$ may be written as follows:

$$
{\tilde{\boldsymbol{\tau}}_{ai}}^*{}_n = \frac{{\boldsymbol{\tau}_{ai}}^* b_n}{h_E^*} = \frac{{\boldsymbol{\tau}_{ai}}^*}{h_E^*}\frac{\sin(n\pi h_E^*)}{n\pi} = {\tilde{\boldsymbol{\tau}}_{ai}}^*\left[1 - \frac{1}{6}(n\pi h_E^*)^2 + \cdots\right] \quad (n = 1, 2, 3, \cdots).
$$

This yields $|{\tilde{\boldsymbol{\tau}}_{ai}}^*{}_1| > |{\tilde{\boldsymbol{\tau}}_{ai}}^*{}_2| > |{\tilde{\boldsymbol{\tau}}_{ai}}^*{}_3| > \cdots$. Thus, along with (24), the lowest mode resonance tends to cause the highest growth rate. Therefore, the band spacing is likely determined by the lowest mode, denoted by the N-th mode, among the possible resonance modes.

Figure 3b shows the relationship between the nondimensional ice-band propagation speed and the nondimensional band spacing. The band spacing in Fig. 3b is evaluated by the lowest internal wave mode N for a given ice-band propagation speed ${\overline{U}_i}^*$. Because (21) indicates that the ice band with the n-th mode internal waves can exist only when ${\overline{U}_i}^* > {\hat{c}_n}^*$, the first mode causes the maximum growth (i.e., $N = 1$) if ${\overline{U}_i}^* > {\hat{c}_1}^*$. If U_i

becomes smaller so that $\hat{c}_2^* < \overline{U}_i^* < \hat{c}_1^*$, the maximum growth occurs with the second mode ($N = 2$), and so on. Therefore, although the ice propagation speed decreases, the resonance does not disappear; however it is switched to the higher-mode wave. This feature is markedly different from the 1.5-layer model, in which resonance no longer occurs place if $c_I^* > \overline{U}_i^*$ (see *Saiki and Mitsudera*, 2016, Fig. 7). This also indicates that the governing equation (15) is always hyperbolic for $\omega^* \geq 1$ (or $\overline{U}_i^* k^* \geq 1$) as long as the wave mode chosen is sufficiently high.

In general, Fig. 3b implies that if the band pattern propagation speed is higher, the band spacing tends to be wider unless the wave mode is switched. In this study, one of our aims is to examine this theory with numerical experiments and satellite image analysis. Note that we restrict our attention to ice bands with a 1–10 km band spacing, in which the hydrostatic approximation is valid.

3 Numerical experiments

To reproduce the ice-band pattern formation and examine the characteristics of ice bands predicted by the theory in the previous section, we performed several numerical experiments. We used the ice-ocean coupled model, based on *Fujisaki and Oey* (2011). The ocean model was based on the Princeton Ocean Model (POM), which employs the primitive equations with hydrostatic as well as Boussinesq approximations (*Mellor et al.*, 2002). The ice model used the elastic-viscous-plastic (EVP) rheology (*Hunke and Dukowicz*, 1997) with ice-collision parameterization (*Sagawa*, 2007). The size of the numerical domain was set to 160 km $\times$ 220 km. Both zonal and meridional boundary conditions were set to be periodic. The horizontal resolution was set at 250 m. The sea bottom was flat, its depth was set to 150 m, and it had 31 levels that were uniformly distributed with a level interval of 5.6 m, except upper and lower two layers for which interval level were 1 m. The parameter values, control experiment settings, and different parameters with respect to the control experiment are listed in Tab. 1, Tab. 2, and Tab. 3, respectively.

3.1 Experiments with an ice edge

3.1.1 Overview of experimental results

We examined ice-band formation in a sea-ice area with the blowing wind using the numerical model. We set the initial stratification as in Fig. 4, referring to the winter Okhotsk

Sea Shelf (*Ohshima et al.*, 2001), where salinity is 32.0 psu at the surface and 33.5 psu at the bottom, and the potential temperature is -1.0 C° at the surface and 0.0 C° at the bottom. Further, the quarter on the left-hand side of this domain was covered by sea ice (see Fig. 6a). That is, there was a distinct ice edge in the initial condition. The initial sea-ice concentration was 0.5 and the ice thickness was 0.5 m. Random noises were not included in the initial condition in this case. Later in Section 5, we examine the effects of ice concentration and ice thickness.

Then, spatially homogeneous wind, which gradually increased from $(U_a, V_a) = (0.0$ $\mathrm{ms}^{-1}, 0.0\ \mathrm{ms}^{-1})$ to $(7.5\ \mathrm{ms}^{-1}, 7.5\ \mathrm{ms}^{-1})$ in one day to prevent numerical shock, was imposed; the wind was kept steady afterward. Here, U_a and V_a are the normal and the parallel components with respect to the initial ice edge of the homogeneous wind, respectively. Note that we do not consider the thermal effects (i.e., the heat flux at the sea surface, sea ice growth, melting, and new ice formation) in this numerical experiment because our main purpose is to understand the dynamical processes of the band formation. This case was considered as the control case.

Figure 6 shows the ice-band formation in the control case. The initial state (Fig. 6a) included an ice edge, and a homogeneous wind was imposed all over this domain. Figure 6b shows clearly that ice bands formed after 6.75 days. Note that the structure of the ice bands depends on the initial distribution of the ice edge shape. In the present case, the initial disturbance at the ice edge was straight and independent of y, and it was robust such that the band patterns were homogeneous with respect to the y-direction.

Next, we investigate the time development of the ice bands and the vertical flow under the ice bands. According to our theory, these vertical flows will keep increasing because of the interaction between the sea ice and the internal waves. Figures 7a, c, and e represent the sea-ice concentration after 3 days, 5 days, and 6.75 days from the initial state, respectively, while Figs. 7b, d, and f represent the vertical flows under ice bands after 3 days, 5 days, and 6.75 days, respectively. From these numerical results, we find that the ice bands gradually grow over time. Correspondingly, the vertical flows of the baroclinic second mode are excited and grow under the ice bands. This is consistent with our theory.

As for the phase relationship between the band structure of the sea-ice concentration and the vertical flows under these bands, the upwelling that occurs forward of each band and the downwelling backward of each band are coupled with the ice bands. Thus, we confirm that the ice-band formation occurs because of the instability due to the interaction between the sea ice and the internal waves; a detailed discussion of the coupling mechanisms can be found in *Saiki and Mitsudera* (2016).

3.1.2 Ice-band scale

Next, we investigated the band spacing change in terms of the wind speed. Figure 8a shows the numerical experiment for $(U_a, V_a) = (6.0\ \mathrm{ms}^{-1}, 6.0\ \mathrm{ms}^{-1})$, and Fig. 8b shows the numerical experiment for $(U_a, V_a) = (9.0\ \mathrm{ms}^{-1}, 9.0\ \mathrm{ms}^{-1})$. It is clearly seen that the band spacing is wider when the wind speed is higher. This result is consistent with the $\mathrm{O}(\epsilon^0)$ solution in Section 2.

Figure 9 compares the theoretical band spacing and the numerical results with respect to the wind speed. Here, referring to (21), we obtain the band spacing

$$\lambda_N = \frac{2\pi}{k_{0N}} = 2\pi \frac{(\overline{U}_i^{\,2} - \hat{c}_N^2)^{1/2}}{f}, \tag{25}$$

where $\hat{c}_N$ denotes the dimensional baroclinic phase speed of the N-th mode, representing the lowest resonant mode, and $f = 2\Omega \sin 50^\circ = 1.12 \times 10^{-4}\ \mathrm{s}^{-1}$. As a typical latitude, we adopted 50°N around the Sea of Okhotsk where a large ice-band area appeared in a satellite image (*Saiki and Mitsudera*, 2016, their Fig. 12c).

The theoretical results coincide well with the numerical results (Fig. 9). For example, because $\overline{U}_i = 0.24$ ms^{-1} for $(U_a, V_a) = (6.0$ ms^{-1}, 6.0 ms$^{-1})$, $\overline{U}_i$ is larger than $\hat{c}_2 = 0.21$ms^{-1}, and hence, the band can couple with the second mode internal waves (i.e., $N = 2$). When $\overline{U}_i$ is slower than the second mode wave with $\hat{c}_2$, however, the resonance is taken over by the third mode internal waves with $\hat{c}_3$. That is, the band spacing is determined by the third mode, $N = 3$, when the wind speed reduces to $(U_a, V_a) = (5.0$ ms^{-1}, 5.0 ms$^{-1})$, or $\overline{U}_i = 0.19$ ms^{-1}. This supports our theory in Section 2 that the maximum growth rate is obtained from the lowest possible resonant mode for a given $\overline{U}_i$.

3.1.3 Wind direction and growth rates

Next, we evaluated the growth rate of the ice band associated with the change in wind direction. The initial setting was the same as in Section 3.1, and we compared four cases in terms of the wind direction θ_a as shown in Figs. 10a to d.

Figures 10b and c (for the case $\theta_a = \pi/4$ and 0, respectively) show that the ice bands develop over time. In contrast, Figs. 10a and d (for the case $\theta_a = \pi/2$ and $\theta_a = -\pi/4$, respectively) do not show ice-band formation except for a band-like structure at the ice edge. Figure 10e depicts the growth rates (day^{-1}) of the vertical-flow strength associated with internal waves with respect to the wind direction θ_a. The growth rate is defined by the growth of the vertical-flow amplitude in the ocean from day 3 to day 4. Figure 10e shows that the growth rate is the highest value when the wind direction turns to the counter-clockwise with respect to the band-propagation direction, which is consistent with the theory. The maximum value of the growth rate was obtained between 20° and 30°, which is approximately 1 day^{-1}. Therefore, ice bands grow in a day with this mechanism, which is consistent with observations (e.g. *Saiki and Mitsudera*, 2016).

3.1.4 Deep ocean

In the numerical experiments in the previous sub-sections, the depth of the ocean was considered to be 150 m because ice bands tend to develop over shallow continental shelves such as those in the Bering Sea (e.g. *Muench et al.*, 1983) and in the East Greenland Current (Fig. 1b). A shallow sea is suitable for the internal wave baroclinic mode formation, because the reflection of vertically propagating waves is sufficiently strong. However, ice bands often appear over deep oceans as well, such as those in the Eurasian Basin in the Arctic Sea (Fig. 1d), the central basin of the Sea of Okhotsk (*Saiki and Mitsudera*, 2016), and the Southern Ocean (*Ishida and Ohshima*, 2009).

In this subsection, we consider ice-band formation in a deep ocean. We do not intend to investigate the band formation again with baroclinic normal modes that are formed by reflection at the ocean bottom. Rather, we show that ice bands can form as long as a strong pycnocline is present below the ocean surface, irrespective of the reflection of the internal waves at the bottom. A strong halocline forms in the polar seas because of sea ice melting and freshwater input due to riverine discharge (e.g. *Davis et al.*, 2016; *Rudels et al.*, 2005; *Mizuta et al.*, 2004). Figure 11a displays the density profile used for a simulation, which mimics the density profile in the Eurasian Basin of the Arctic Sea, where a strong density gradient between the depths of 40 m and 110 m represents a halocline. Stratification below the halocline was characterized by $N_B = 0.0045$ s^{-1} in this simulation. The depth of the ocean bottom was 2150 m. A wind of $(U_a,\ V_a) = (7.5$ ms^{-1}, 7.5 ms$^{-1})$ was imposed. The initial ice concentration was 0.5, as in Fig. 6.

Figures 11b and c indicate that ice bands form in a manner similar to the previous cases (see, e.g., Fig. 7), although the internal waves are confined to the upper ocean. An ice band is generated at the leading edge of the ice zone initially (Fig. 11b). Then, an internal wave, which propagates below the sea ice along the halocline, induces ice bands one after another (Fig. 11c). We also conducted experiments with various N_B values below the halocline and obtained similar results. This implies that ice bands form in deep seas when the halocline below sea ice is strong, which frequently occurs in the polar seas.

3.2 Ice-band pattern emerging from random initial ice concentration

3.2.1 Ice-band pattern formation

Here, we discuss the ice-band pattern formation from a random initial condition. This is different from the previous step-like ice-edge case in which the long axis of the ice band was parallel to the ice edge. Figure 12a shows an experiment with a homogeneous wind $(U_a, V_a) = (7.5\ \mathrm{ms}^{-1},\ 7.5\ \mathrm{ms}^{-1})$ blowing over a sea-ice field where the initial ice concentration is random. There were no initial ice edges in this case. Other parameters including stratification are the same as those in the control case.

In this case, the ice-band pattern with the maximum growth rate gradually emerges from the white noise, as shown in Fig. 12b. This feature directly corresponds to the band formation due to resonance discussed in Section 2. Further, the vertical section of the vertical velocity field in Fig. 12c shows that the second mode internal waves are excited with this ice-band formation. $\overline{U}_i$ is typically 0.25 ms^{-1}, and hence, this is consistent with Fig. 9. The band spacing is approximately 10 km, and growth rate from day 3 to day 4 is approximately 1.37 day^{-1}. This band spacing and the growth rate are similar to those in the ice-edge case shown in Fig. 6 and Fig. 10. Therefore, we conclude that as long as the initial perturbed field is present, the ice band is generated by resonance even though there is no initial ice edge.

3.2.2 Plume-like ice-band pattern in MIZs

Next, we consider the formation of the plume-like ice bands. They are observed in the MIZs in the East Greenland Current (Fig. 1b) and the Sea of Okhotsk. Here, we reproduced these plume-like ice-band structures that form almost perpendicularly to the ice edge in the MIZs.

We consider this problem as the band-pattern formation problem from a random initial ice concentration, although the ice edge is present in this case. An example is shown in Fig. 13. The area spanning $0 < x < 37$ km was set as the initial sea-ice area with the white noise, and the area $x > 37$ km was set as the open water area. Then, a homogeneous wind $(U_a, V_a) = (7.5 \text{ ms}^{-1}, -7.5 \text{ ms}^{-1})$ was imposed all over this domain. Note that the wind is not favorable for band formation if white noise is not included (see Fig. 10d). We set the boundary condition such that the sea ice inflow was from the left-hand side of the domain at $x = 0$, and the outflow of this sea ice was to the right-hand side of the domain with a free-drift condition. Figure 13b displays the ice bands after 10 days. We observe that plume-like ice bands develop across the ice edge, similar to the observations in Fig. 1b, d. The direction of the long axes is consistent with that of maximum growth (24). Therefore, the plume-like ice bands are well explained by the pattern formation due to the wind.

4 Validation by satellite observations

In this section, the relationship between the wind speed and the band spacing seen in satellite images is compared with the theoretical and numerical results. We are particularly interested in the comparison with the dispersion relationship of the internal waves. We collected ice-band information for the Sea of Okhotsk and the East Greenland Current using images of MODIS and AVHRR. The ice-band formation in the Bering Sea discussed by *Muench and Charnell* (1977) was also included.

To quantitatively compare the theoretical results with the ice bands in the real ocean, we manually analyzed satellite images, according to the following procedures:

1. First, we checked MODIS (the East Greenland Current) and AVHRR (the Sea of Okhotsk) images, whose horizontal resolutions are 250 m and 1.1 km, respectively.

2. Next, the images were rotated, so that the band axis was aligned to the pixels by using a software called Lightroom 4.2. Then, the band spacing was defined by measuring the length between the center of one band and that of the adjacent band. Further, a mean band spacing in the target area was calculated if at least five bands were found in the target area (an example is shown in Fig. 14).

3. Finally, we compared the above mean band spacing with six hourly mean wind speeds at 10 m above the sea surface (U10) of the ECMWF Interium. The wind one day before was used because the growth of ice bands was considered. Here, we used about the order 100 images.

Figure 15a displays the relationship between the wind speed and the band spacing. Ice-band spacings in the Bering Sea by *Muench and Charnell* (1977) are also plotted in Fig. 15a. We find that as the wind speed increases, the band spacing becomes wider in general, which is consistent with the theory. Further, the results of our numerical experiments are plotted in Fig. 15a for reference, in which the model stratification mimics that of the Bering Sea (Fig. 15b). As this figure indicates, the numerical solution also represents the observed values well. The band spacings are limited by $\lambda_{max} = 2\pi\overline{U}_i/f$, indicated by the solid line in Fig. 15a, where $\overline{U}_i$ is evaluated by 2.5% of the wind speed according to *Kimura and Wakatsuchi* (2000); λ_{max} represents the maximum band width associated with the internal inertial gravity waves, which is derived from the inertial frequency.

Figure 16 shows the frequency evaluated by $\overline{U}_i k$ comparing with the dispersion relationship of the internal inertia-gravity waves. This shows that most of the observed normalized frequencies exceed unity. Further, frequencies evaluated by $\overline{U}_i k$ are distributed above the inertial frequency. Therefore, 10-km-scale ice bands are explained well by our theory, incorporating the internal inertia-gravity waves. Further, because the internal wave frequency is close to the inertial frequency, the hydrostatic approximation incorporated in the theory and numerical experiments is valid. In conclusion, 10-km-scale ice bands in the MIZs in the polar seas are well explained by the resonance discussed in this paper.

We also reexamine the relationship between the band spacing and the wind speed over the Southern Ocean discussed by *Ishida and Ohshima* (2009) (see their Fig. 7b). Figure 17 shows the wind vs. band spacing relationship of the observed values in *Ishida and Ohshima* (2009). The black dashed lines in Figs. 17b and c denote the relationship $\lambda_{max} = 2\pi\overline{U}_i/f$, where $\overline{U}_i$ is scaled by 0.02 $|\boldsymbol{U}_a|$ and f is the Coriolis parameter at 62° S. All ice bands in their paper were observed from August to December.

The upper layer structure changes from the mixed layer in winter to a seasonal pycnocline in spring in the Southern Ocean. We modeled the winter stratification by a blue curve profile in Fig. 17a, and the spring stratification by a red curve profile, according to the study of *Wong and Riser* (2011). In both seasons, band spacings tend to increase as the wind increases (Figs. 17b and c), which is consistent with the theory. The comparison of Figs. 17b and c shows that the band spacing is substantially longer in winter than in spring. This suggests that the band spacing would depend on the seasonal density profiles as modeled in Fig. 17a. Further, maximum widths λ_{Emax} evaluated by the baroclinic phase speed $\hat{c}_N$ with the maximum growth rate, are also displayed as white dashed lines in Fig. 17b (Fig. 17c) for winter (spring). In both winter and summer, most of the observed band spacings appear below the white dashed lines (i.e., λ_{Emax}) for a given wind speed. That is, the band spacings are evaluated quite well by λ_{Emax}. Because λ_{Emax} in spring is shorter than λ_{Emax} in winter (compare Figs. 17b and c), it is suggested that the seasonal difference in band spacings observed by *Ishida and Ohshima* (2009) could be partly attributed to the density profile change from the mixed-layer type in winter to the surface pycnocline type in spring.

5 Sensitivity studies

In this section, we discuss various effects that control ice-band formation, such as ice concentration, ice thickness, ice stresses, wind temporal change and the Earth's rotation. For such purposes, we carried out sensitivity experiments in comparison with the control experiment in Section 3 (mean ice concentration $\overline{A} = 0.5$; ice thickness $d = 0.5$ m; ice-water drag coefficient; $C_{Diw} = 6.0 \times 10^{-3}$; homogeneous wind speed $(U_a, V_a) = (7.5, 7.5)$ m s^{-1};

Coriolis parameter $f = 2\Omega \sin 50^\circ$ s^{-1}).

5.1 Ice concentration

In this subsection 5.1, we examined the effects of varying ice-concentration for the ice-band pattern formation. In our theory, since it is linear, the ice-band patterns are formed as long as there are initial perturbations. Thus, we carried out an experiment using a domain covered with the mean ice concentration of 0.9 with random noise, where $\overline{A} = 0.8 + 0.2 \times rand$; $rand$ is a function of random noise where $0 < rand < 1$ (Fig. 18a, b). As a result, we confirmed that the ice-band patterns with the second baroclinic mode internal waves emerge because of a homogeneous wind (Fig. 18c). Although the growth rate of ice-band development is less than that in the case of Fig 13b because of the high ice concentration, the band formation occurs even for $\overline{A} = 0.9$ as a result of the resonance.

Next, we investigated the effects of ice concentration when the ice field includes both an ice edge and random noise, by varying $\overline{A}$ and θ_a. In these experiments, we focused on the competition between perturbations generated by the ice edge and the perturbations due to the random noise; the ice-band pattern was parallel to the ice edge for the former, whereas for the latter, the pattern was determined by the perturbation of the maximum growth for a given wind direction. Here, we examined cases when the wind direction θ_a is negative in terms of the initial ice edge, in a manner similar to that in Fig. 10d, because the plume-like band pattern in the East Greenland Current, the Arctic Sea (Fig. 1b), and the Sea of Okhotsk (*Saiki and Mitsudera*, 2016) occurs owing to a northwesterly wind, which corresponds to a negative θ_a. Note that the wind direction of $\theta_a \lesssim -\pi/6$ is not favorable for the band-pattern growth that is parallel to the ice edge (see Fig. 10d, e).

There are various patterns depending on $\overline{A}$ and θ_a as in Fig. 19. When $\overline{A} = 0.9$, the ice-band patterns parallel to the ice edge (denoted by $\diamondsuit$) occur when θ_a is close to zero, while the band pattern does not occur for $\theta_a \lesssim -\pi/4$ (denoted as $\times$). That is, the band pattern originating from the random initial noise does not emerge for $\overline{A} = 0.9$. This is different from the case without an ice edge, in which the band pattern is manifested even when $\overline{A} = 0.9$. As $\overline{A}$ decreases to $\overline{A} = 0.75$, ice-band patterns appear over the interior of the sea-ice area. This represents the co-existence of the ice edge effect and a random noise effect. As $\overline{A}$ decreases further to 0.5, plume-like band patterns (denoted by $\bigcirc$) appear for $-\pi/2 \leq \theta_a \lesssim -\pi/4$. The case of Fig. 13 ($\theta_a = -\pi/4$, $\overline{A} = 0.5$) falls under this category. In this case, perturbations generated from random noise dominate over the perturbations from the ice edge. As for $\theta_a \gtrsim -\pi/8$, ice bands generated from the ice edge co-exist with those generated from random noise (denoted by $\square$).

These experiments show that the plume-like band pattern occurs when the ice concentration is relatively low near the ice edge. In reality, this situation is likely realized in MIZs for off-ice winds because sea ice drifts to the open water and melts, resulting in reduction of ice concentration near the ice edge. Further, wind direction tends to be $\theta_a \simeq -\pi/4$ with respect to the ice edge in the East Greenland Current and the Sea of Okhotsk because of the dominance of the northwesterly monsoon wind. As shown by Fig. 19, the ice band patterns emerging from random noise may well dominate in this case, resulting in the plume-like band formation.

5.2 Effect of ice thickness

Thus far, we assumed that the ice thickness d is 0.5 m. Here, we investigate the effects of the ice thickness on ice-band formation. Figure 20 displays the case when the ice thickness is 0.1 m as well as for 1 m. The angle between the wind direction and the propagation direction, i.e., θ_a, appears larger for the 1-m-thick case than that for the 0.1-m-thick case. This result is consistent with the dependence of the turning angle $\delta\theta$ between $\boldsymbol{\tau}_{iw}$ and $\boldsymbol{\tau}_{ai}$

on d. The equation of motion for the freely drifting sea ice is written as (*Leppäranta*, 2005; *Saiki and Mitsudera*, 2016)

$$\boldsymbol{\tau}_{ai} = \boldsymbol{\tau}_{iw} + \rho_i f d \boldsymbol{k} \times \boldsymbol{u}_i,$$

where $\boldsymbol{u}_i$ is the ice drift velocity, and ρ_i is the ice density. Therefore, $\delta\theta$ increases with d because of the Coriolis force. As (23) indicates, the favorable wind direction θ_a is expected to increase with increasing $\delta\theta$. The numerical results in Figs. 20a and b are thus consistent with the effect of the ice thickness as indicated in (23).

5.3 Drag coefficients

In this subsection, we examine the ice-band patterns change with respect to varying ice–water drag coefficients C_{Diw}. We used $C_{Diw} = 6.0 \times 10^{-3}$ as the typical value in Section 3. According to *Lu et al.* (2011), the ice–water drag coefficient values ranged from 1.0×10^{-3} to 2.0×10^{-2}.

Figure 21 depicts the relationship between C_{Diw} and the band spacings, while C_{Dai} is kept constant, where C_{Dai} is the air–ice drag coefficient. Since $|\overline{\boldsymbol{U}}_i| \simeq \sqrt{\rho_a C_{Dai}/\rho_w C_{Diw}} |\overline{\boldsymbol{U}}_a|$, changes in C_{Diw} correspond to changes in $\overline{\boldsymbol{U}}_i$ for a given C_{Dai}. Therefore, the band spacing varies with the change in C_{Diw} change. The numerical results correspond well with the theory (Fig. 21). The resonance mode shifted from the first to the third ones in the range of C_{Diw} from 1.0×10^{-3} to 2.0×10^{-2}. We used $C_{Diw} = 6.0 \times 10^{-3}$ in Section 3, with which the band-propagation speed $\overline{U}_i$ was 0.29 ms^{-1}. The ice-drift speed was estimated well by $|\overline{\boldsymbol{U}}_i| \simeq \sqrt{\rho_a C_{Dai}/\rho_w C_{Diw}}|\overline{\boldsymbol{U}}_a|$, which gives approximately $0.025|\overline{\boldsymbol{U}}_a|$ ms^{-1} using Tab. 1 values, where C_{Dai} is 3.0×10^{-3} (*Fujisaki et al.*, 2010). In reality, C_{Dai} may increase if C_{Diw} is larger, because generally, the roughness on the bottom of sea ice reflects the roughness on the surface of sea ice. Therefore, the empirical relationship of $|\overline{\boldsymbol{U}}_i| \simeq 0.025|\overline{\boldsymbol{U}}_a|$ ms^{-1} in Section 4 could hold for a range of the drag coefficient, with $C_{Dai}/C_{Diw} \simeq 0.5$.

We also consider the relationship between C_{Dai} and C_{Daw}. In general, C_{Dai} is larger than C_{Daw}, and the band formation occurs in this case. However, if an open water is sufficiently rough, for example, because of large-amplitude wind waves, C_{Daw} could be larger than C_{Dai}. Therefore, we carried out an experiment with $C_{Daw} > C_{Dai}$, and found that the ice-band patterns did not form in this case (figure not shown). This is because the sea-surface convergence/divergence patterns associated with the ice drift were opposite to those of the resonant interaction depicted in Fig. 8 of *Saiki and Mitsudera* (2016).

5.4 Temporally varying wind

Next, we assumed that the wind varies with time such that $|\boldsymbol{V}_a| = V_a \sin^2(\omega t/2)$, where the period ($= 2\pi/\omega$) was set at 2, 4, and 8 days, and V_a was set to 10 ms^{-1}. This was motivated by an observation in which ice bands were formed by a passage of a synoptic low pressure system (*Saiki and Mitsudera*, 2016). Figure 22 shows that the ice-band patterns, similar to the previous steady-wind case, appear for winds with 4- and 8-day periods. The band spacing of 10 km was estimated well by the resonant condition (21) with a mean wind speed of 5 ms^{-1}. However, if the period of the wind variation was shorter, e.g., $2\pi/\omega = 2$ days, a pattern parallel to the wind becomes dominant. The effects of temporally varying wind with higher frequency needs to be studied further, although the theory is likely applicable to synoptic time scales.

5.5 Coriolis parameter -effects of Earth's rotation-

Here, we investigate the effects of the Earth's rotation on the band spacing. A control value of the Coriolis parameter was set to be $f = 2\Omega \sin 50^\circ$ s^{-1} (Tab. 1), which targets the Sea of Okhotsk around 50° N.

Figure 23 shows the results of this sensitivity study for varying f. The band spacing becomes narrower as the latitude increases, consistent with Eq. (25), where $\lambda_N = 2\pi(\overline{U}_i^2 - c_N^2)^{1/2}/f$. Nevertheless, the band spacing does not change considerably in the high latitude range, where sea ice can exist.

For the non-rotational limit where $f \to 0$, the dispersion relationship in (19) may be rewritten as

$$\omega_{0n}^* = \hat{c}_n{}^* k_{0n}^*. \tag{26}$$

Saiki and Mitsudera (2016) pointed out that ice bands which of the 10-km-scale do not form unless the Earth's rotation is present, because resonance in this case can occur only when $k_{0n}^* = 0$. Figure 24 confirms their statement. A Couette-like shear flow forms in response to wind forcing. The horizontal scale of the vertical flows is related to the distance between the two ice edges. Therefore, no interaction occurs between the internal waves and ice bands with a finite wavelength inside the ice zone.

6 Conclusion

In this study, we presented a new theory on the ice-band formation for continuously stratified ocean, which extended our previous work based on the 1.5-layer ocean (*Saiki and Mitsudera*, 2016). The theory provides a plausible explanation for the formation of the 10-km-scale ice bands, which are widely observed in the MIZ. The core idea is that resonant interaction between divergence/convergence in the sea ice motion field and that arising from internal inertia-gravity wave forms band patterns. A distinct difference between the continuously-stratified-ocean model and the 1.5-layer model is the existence of an infinite number of internal wave modes in the former. We found that there is no minimum band propagation speed $\overline{U}_i$ for the ice-band pattern formation as for the continuously stratified ocean models. That is, although $\overline{U}_i$ becomes too slow for one mode to be resonant, the higher modes still maintain the resonant condition and contribute to the ice-band formation. This characteristic is important for applying this theory to observed ice bands.

For the turning angle, we numerically showed that the maximum growth rate was observed when the wind direction turns to the counter-clockwise (clockwise) slightly with respect to the band-propagation direction in the Northern (Southern) Hemisphere. This is consistent with the theory as well as satellite images (see e.g., Fig. 1).

An important idea in this study was to consider ice-band formation as a pattern formation problem. This implies that the band pattern emerges from a random initial field as a result of instability, or resonant interaction, in the ice-ocean coupled system. We proved this by conducting numerical experiments in which the ocean was covered by sea ice with an initial random ice concentration, and a homogeneous wind blowing on it. As expected, ice bands emerged from this non-structured initial condition. This result is important for explaining the plume-like band formation across the ice edge of MIZs, as shown in Fig. 1. Indeed, a numerical experiment in Fig. 13, which includes a step-like initial ice edge as well as white noise, shows the generation of the plume-like band pattern across the initial ice edge when the direction of the wind is not favorable to perturbations caused by the ice edge. That is, the plume-like band forms because of the initial random noise, not because of the initial ice edge.

Next, we analyzed the satellite images of the polar oceans such as those in the Sea of Okhotsk, Bering Sea, and East Greenland Current and validated that the band spacing becomes wider when the wind speed increases in the real ocean. It was also shown that the internal wave frequency interacting with 10-km-scale ice bands is close to the inertial frequency, which is also consistent with the theory. Further, the theory suggests that the seasonal difference in ice-band spacings in the Southern Ocean could be attributed to the upper ocean changes from the deep mixed layer in winter to the surface seasonal pycnocline in spring.

Finally, we carried out sensitivity experiments to discuss various effects for ice-band pattern formation such as ice concentration, ice thickness, ice drags, temporal wind changes, and Earth's rotation. It was found that ice band forms when (1) ice field contains random noise, (2) the air–ice drag is larger than the air–water drag, (3) wind blows with a longer period than a synoptic time scale, and (4) the Earth's rotation is present. If an initial sea-ice area has the ice edge, the plume-like ice-band pattern becomes dominant when the ice concentration is relatively small, say, $\overline{A} = 0.5$. In consequence, we confirmed that the plume-like 10-km-scale ice-band pattern emerges because of the northwesterly wind as in the case of the East Greenland Current, the Sea of Okhotsk, and the Arctic Sea.

In the present study, we did not deal with surface waves and thermodynamics but focused on the dynamical processes of the band pattern formation. Fetch-limited surface waves can gather ice floes by wave radiation stresses and enhance the band structure (*Wadhams*, 1983). This implies that once the ice band scale is determined by the ice-ocean resonance as discussed in this study, the band structure may be further enhanced by the wave radiation-stress mechanism. Further, surface waves fracture pack ice into small-sized ice floes in MIZs (*Toyota et al.*, 2006; *Toyota et al.*, 2010) and promote ice melting (*Steele*, 1992). The thermodynamical processes associated with ice-band formation should be considered in future studies. In particular, melting reduces ice concentration in MIZs, which is a favorable condition for the plume-like ice-band formation. Once open waters are created by the ice-band generation as discussed in this study, surface waves in the open ocean can enter the interior of MIZs and break interior pack ice into small ice floes further. As a result, melting may be promoted and the reduction in the ice concentration may be enhanced in the interior of sea-ice area. It is well-known that the sea ice in the Arctic Sea melts rapidly, and it is difficult to predict by any numerical model (*Stroeve et al.*, 2007; *Rosenblum and Eisenman*, 2017). Thus, it is necessary to consider the melting processes and parameterization in MIZs further.

According to CMIP6 model simulations, there is a high chance that the Arctic Ocean would become ice-free in summer in decades to come (*Notz et al.*, 2020). In this future scenario, the seasonal ice zone in the Arctic would expand considerably, and the expansion of the area where the ice edge sweeps in a seasonal cycle would likely follow. It is conceivable that, in a freezing part of this seasonal cycle, the formation process of the ice band and its spatial distribution would have significant impacts on the salt flux to the ocean and the turbulent heat flux to the atmosphere. As such, we envision that integrated studies on the air-sea-ice interaction in the MIZ are of high importance for better understanding of future climate.

Appendix 1 : Specific form of $\boldsymbol{\tau}'$

As depicted in Fig. 2a, the air–ice and ice–water stresses are defined as

$$\boldsymbol{\tau}_{iw} = |\boldsymbol{\tau}_{iw}|(\boldsymbol{i}\cos\theta_i + \boldsymbol{j}\sin\theta_i),$$

$$\boldsymbol{\tau}_{ai} = |\boldsymbol{\tau}_{ai}|(\boldsymbol{i}\cos\theta_a + \boldsymbol{j}\sin\theta_a),$$

$$\delta\theta = \theta_a - \theta_i,$$

where $\boldsymbol{i}$ and $\boldsymbol{j}$ are unit vectors in the x and y directions, respectively. In general, $|\boldsymbol{\tau}_{iw}| \simeq |\boldsymbol{\tau}_{ai}|$, and $\delta\theta << 1$, because the effects of f are small for drifting ice (*Leppäranta*, 2005). Similarly, the air–water stress is written as

$$\boldsymbol{\tau}_{aw} = |\boldsymbol{\tau}_{aw}|(\boldsymbol{i}\cos\theta_a + \boldsymbol{j}\sin\theta_a).$$

Suppose that sea the surface is covered by ice with concentration A (Fig 2b). We assume that the ice roughness is homogeneous in the model domain, so that the perturbation of the sea surface stress is retrieved from the perturbation in the ice concentration; that is,

$$
\begin{aligned}
\boldsymbol{\tau}' &= A'\boldsymbol{\tau}_{iw} - A'\boldsymbol{\tau}_{aw} \\
&= A'\boldsymbol{i}[(|\boldsymbol{\tau}_{iw}|\cos\delta\theta - |\boldsymbol{\tau}_{aw}|)\cos\theta_a + |\boldsymbol{\tau}_{iw}|\sin\theta_a\sin\delta\theta] \\
&+ A'\boldsymbol{j}[(|\boldsymbol{\tau}_{iw}|\cos\delta\theta - |\boldsymbol{\tau}_{aw}|)\sin\theta_a - |\boldsymbol{\tau}_{iw}|\sin\theta_a\cos\delta\theta].
\end{aligned}
$$

Noting that $|\boldsymbol{\tau}_{iw}| \simeq |\boldsymbol{\tau}_{ai}|$ because we assume the free drifting condition and the effects of the Coriolis force are small (*Leppäranta*, 2005), we obtain

$$
\boldsymbol{\tau}' = A'\left[\left(\frac{\Delta\boldsymbol{\tau}}{|\boldsymbol{\tau}_{ai}|}\tau_{ai}^{x} + (\sin\delta\theta)\tau_{ai}^{y}\right)\boldsymbol{i} + \left(\frac{\Delta\boldsymbol{\tau}}{|\boldsymbol{\tau}_{ai}|}\tau_{ai}^{y} + (\sin\delta\theta)\tau_{ai}^{x}\right)\boldsymbol{j}\right], \tag{A1}
$$

where

$$
\Delta\boldsymbol{\tau} = |\boldsymbol{\tau}_{iw}|\cos\delta\theta - |\boldsymbol{\tau}_{aw}| \simeq |\boldsymbol{\tau}_{ai}|\cos\delta\theta - |\boldsymbol{\tau}_{aw}|,
$$

$$
|\boldsymbol{\tau}_{iw}|\cos\theta_a \simeq |\boldsymbol{\tau}_{ai}|\cos\theta_a = \tau_{ai}^{x},
$$

$$
|\boldsymbol{\tau}_{iw}|\sin\theta_a \simeq |\boldsymbol{\tau}_{ai}|\sin\theta_a = \tau_{ai}^{y}.
$$

Therefore, the evolution equation of the internal gravity waves is written as

$$\left(\frac{\partial^2}{\partial t^2}+f^2\right)\frac{\partial \tilde{\eta}_n}{\partial t}-\hat{c}_n{}^2\frac{\partial}{\partial t}\frac{\partial^2 \tilde{\eta}_n{}^2}{\partial x^2}=-h_n\left(\frac{\partial^2 \tilde{\tau}_n{}^x}{\partial t \partial x}+f\frac{\partial \tilde{\tau}_n{}^y}{\partial x}\right), \tag{A2}$$

666 where

$$\tilde{\boldsymbol{\tau}}_n=\tilde{\tau}_n{}^x\boldsymbol{i}+\tilde{\tau}_n{}^y\boldsymbol{j}=\frac{\boldsymbol{\tau}' b_n}{\rho_w h_E},$$

where $\boldsymbol{\tau}'$ is given by (A1), and

$$b_n=\frac{1}{D}\int_{-h_E}^{0}\hat{p}_n dz. \tag{A3}$$

667 (A2) is the same as (15), where $|\Delta\boldsymbol{\tau}|/|\boldsymbol{\tau}_{ai}|$ in (A1) is equivalent to $\delta_d{}^*$.

Appendix 2 : **Derivation of the characteristic equation**

The non-dimensional equations corresponding to (15) and (17) yield

$$\frac{\partial}{\partial t^*}\left[\left(\frac{\partial^2}{\partial^2 t^{*2}}+1\right)-\hat{c}_n^{*\ 2}\frac{\partial^2}{\partial^2 x^{*2}}\right]\tilde{\eta}_n^*$$

$$=-\,h_n^*\left[\frac{\partial^2 A'}{\partial t^*\partial x^*}\left(\delta_d{}^*\tilde{\tau}_{ai}^{x}{}_n^* + (\sin\delta\theta)\tilde{\tau}_{ai}^{y}{}_n^*\right)+f\frac{\partial A'}{\partial x}\left(\delta_d{}^*\tilde{\tau}_{ai}^{y}{}_n^* - (\sin\delta\theta)\,\tilde{\tau}_{ai}^{x}{}_n^*\right)\right], \qquad \text{(A4)}$$

and

$$\frac{\partial A'}{\partial t^*}+\overline{U}_i{}^*\frac{\partial A'}{\partial x^*}-\sum_{m=1}^{\infty}\frac{\overline{A}p_m(0)}{h_m^*}\frac{\partial\tilde{\eta}_m{}^*}{\partial t}=0. \qquad \text{(A5)}$$

668 Substituting a plane wave solution

$$\begin{pmatrix} A' \\ \\ \tilde{\eta}_n{}^* \end{pmatrix} = \begin{pmatrix} A'_0 \\ \\ \tilde{\eta}_{0n}^* \end{pmatrix} e^{i(k^*x^*-\omega^*t^*)}$$

in (A4) and (A5), we obtain

$$\begin{aligned}
&\omega^*[(1-\omega^{*2}) + \hat{c}_n^{*2} k^{*2}]\tilde{\eta}_{0n} \\
= \quad & h_n{}^*[i\omega^* k^*(\delta_d{}^* \tilde{\tau}^x_{ai}{}^*_n + (\sin\delta\theta)\tilde{\tau}^y_{ai}{}^*_n) - k^* f(\delta_d{}^* \tilde{\tau}^y_{ai}{}^*_n + (\sin\delta\theta)\tilde{\tau}^x_{ai}{}^*_n)]A_0',
\end{aligned}$$

and

$$(-\omega^* + k^*\overline{U}_i{}^*)A_0' + \sum_{m=1}^{\infty} \frac{\overline{A}p_m(0)}{h_m^*}\omega^*\tilde{\eta}_{0m}^* = 0.$$

If we rewrite

$$\begin{aligned}
a_m &= (1-\omega^{*\,2}) + \hat{c}_m{}^{*\,2} k^{*\,2}, \\
b_m &= -h_m{}^* \frac{k^*}{\omega^*}[i\omega^*(\delta_d{}^* \tau^x_{ai}{}^*_m + (\sin\delta\theta)\tilde{\tau}^y_{ai}{}^*_m) - f(\delta_d{}^* \tau^y_{ai}{}^*_m + (\sin\delta\theta)\tilde{\tau}^x_{ai}{}^*_m)] \\
\alpha_m &= \frac{\overline{A}p_m(0)}{h_m^*}\omega^*, \\
\beta &= \overline{U}_i{}^* k^* - \omega^*,
\end{aligned}$$

then the eigenvalues are obtained by solving

$$
\begin{vmatrix}
a_1 & 0 & 0 & \dots & & & b_1 \\
0 & a_2 & 0 & & & & b_2 \\
0 & 0 & \ddots & & & & \vdots \\
\vdots & & & a_m & & & b_m \\
 & & & & \ddots & & \vdots \\
 & & & & & a_n & b_n \\
\alpha_1 & \alpha_2 & \dots & \alpha_m & \dots & \alpha_n & \beta
\end{vmatrix}
= a_1
\begin{vmatrix}
a_2 & 0 & \dots & b_2 \\
0 & \ddots & & \vdots \\
\vdots & & a_n & b_n \\
\alpha_2 & \dots & \alpha_n & \beta - \frac{\alpha_1 b_1}{a_1}
\end{vmatrix}
= \cdots
$$

$$
=\beta \left(\prod_{m=1}^{\infty} a_m \right) \left(1 - \sum_{m=1}^{\infty} \frac{\alpha_m b_m}{a_m \beta} \right) = 0, \tag{A6}
$$

where $\prod$ denotes an infinite product. Here, $a_n = 0$ represents the n-th mode wave propagation, whereas $\beta = 0$ represents the band propagation. If the n-th mode waves are resonant with the ice-band propagation so that $a_n \to 0$ and $\beta \to 0$ simultaneously, then we obtain

$$
a_n \beta - \alpha_n b_n \simeq 0.
$$

This yields (18) in the text.

Acknowledgements. We would like to thank for Drs. K. I. Ohshima, H. Yamaguchi, M. Leppäranta, K. Shirasawa, T. Nakanowatari, M. Matsumura, S. Aoki, H. Hasumi, T. Takao, and Y. Komuro for helpful comments and discussions. We would like to thank two anonymous reviewers for their effective comments and suggestion to improve our manuscript. The support from the Pan-Okhotsk Research Center members are greatly appreciated. Our numerical results were obtained with the Pan-Okhotsk Information System. Satellite images from the Kitami Institute of Technology and National Aeronautics and Space Administration (NASA) were used to analyze the data. This work was supported by KAKENHI Nos. 22106001, 26247076, 26247080, 15H05825, and 17H01156. English writing is supported by Editage.

REFERENCES

Broecker, W. S., 2010, The Great Ocean Conveyor: Discovering the Trigger for Abrupt Climate Change, *Princeton Univ. Press*, Princeton.

Davis, P.E.D., C. Lique, H. L. Johnson, and G. D., Guthrie, 2016, Competing effects of elevated vertical mixing and increased freshwater input on the stratification and sea ice cover in a changing Arctic Ocean. *J. Phys. Oceanogr.*, doi:10.1175/JPO-D-15-0174.1.

Dee, D. P., Uppala, S. M., Simmons, A. J., et al., 2011, The ERA-Interim reanalysis: configuration and performance of the data assimilation system, *Q.J. ROYAL. MET. SOCIETY.*, 137(656), 553–597.

Fujisaki, A., and L. Y. Oey, 2011, Formation of ice bands by winds, *J. Geophys. Res.*, 116, C10015.

Fujisaki, A., H. Yamaguchi, H. Mitsudera, 2010, Numerical experiments of air–ice drag coefficient and its impact on ice-ocean coupled system in the Sea of Okhotsk, *J. Ocean Dyn.*, 60 (2) (2010), pp. 377-394.

Gascard, J. C., J. Zhang, and M. Rafizadeh, 2019, Rapid decline of Arctic sea ice volume: Causes and consequences, *The Cryosphere Discuss.*, https://doi.org/10.5194/tc-2019-2, 2019.

Ishida, K., and K. I. Ohshima, 2009, Ice-band characteristics of the Antarctic seasonal ice zone observed using MOS MESSR images, *Atmos – Ocean*, 47(3), 169–183, doi:10.3137/OC300.2009.

Kawaguchi, Y., S. Nishino, J. Inoue, K. Maeno, H. Takeda, K. Oshima, 2016, Enhanced diapycnal mixing due to near-inertial waves propagating through an anticyclonic eddy in the ice-free Chukchi Plateau, *J.Phys.Oceanogr.*, 46 (8), 2457–2481.

Kimura, N., and M. Wakatsuchi (2000), Relationship between sea-ice motion and geostrophic wind in the Northern Hemisphere, *J. Geophys. Res. Lett.*, 27, 3735–3738.

Leppäranta, M. 2005, *The Drift of Sea Ice*, Springer.

Lu, P., Z.Li, B.Cheng, and M.Leppranta, 2011: A parameterization of the ice?ocean drag coefficient. J. Geophys. Res.,116, C07019, doi:10.1029/2010JC006878.

Manucharyan, G. E., and Thompson, A. F., Submesoscale sea ice?ocean interactions in marginal ice zones, *J. Geophys. Res.*, 2017, *Oceans*, 122(12), 9455-9475.

McPhee, M. G., 1979, The effect of the oceanic boundary layer on thr mean drift of pack ice: Application of a simple model, , *J. Phys. Oceanogr.*, 9, 388–400.

McPhee, M. G., 1982, Sea ice drag laws and simple boundary layer concepts including application to rapid melting, *Rep.* 82-4, 17 pp., U.S. Army Cold Reg. Res. and

Eng. Lab., Hanover, N.H.

McPhee, M. G., 1983, Turbulent heat and momentum transfer in the oceanic boundary layer undes melting pack ice, *J. Geophys. Res.*, 88, 2827–2835.

McPhee, M. G., and L. H. Kantha, 1989, Generation of internal waves by sea ice, *J. Geophys.Res.*, 94, 3287–3302.

Mellor, G., S. Hakkinen, T. Ezer, and R. Patchen, 2002, A generalizationof a sigma coordinate ocean model and an intercomparison of model vertical grids, in *Ocean Forecasting : Conceptual Basis and Applications*, edited by N. Pinardi and J. D. Woods, pp. 55–72, Springer, Berlin.

Mizuta, G., and N. G. Hogg, 2004, Structure of the circulation induced by a shoaling topographic wave. *J. Phys. Oceanogra.*, 34, 1793-1810.

Muench, R. D., and R. L. Charnell., 1977, Notes and correspondence observations of medium-scale features along the seasonal ice edge in Bering Sea, *J. Phys. Oceanogra.*, 7, 602–606.

Muench, R. D., P. H. LeBlond, and L. E. Hachmeister, 1983, On some possible interactions between internal waves and sea ice in the marginal ice zone, *J. Geophys. Res.*, 88 (C5), 2819–2826.

Notz, D., Dorr, J., Bailey, D. A., Blockley, E., Bushuk, M., Debernard, J. B., Dekker, E., DeRepentigny, P., Docquier, D., Fuckar, N. S., Fyfe, J. C., Jahn, A., Holland, M., Hunke, E., Iovino, D., Khosravi, N., Massonnet, F., Madec, G., O'Farrell, S., Petty, A., Rana, A., Roach, L., Rosenblum, E., Rousset, C., Semmler, T., Stroeve, J., Tremblay, B., Toyoda, T., Tsujino, H. and Vancoppenolle, M., 2020, Arctic sea ice in CMIP6, *Geophys. Res. Lett.*, 47., e2019GL086749.

Ohshima K. I., G. Mizuta, M. Itoh, Y. Fukamachi, T. Watanabe, Y. Nabae, K. Suehiro, and M. Wakatsuchi, 2001, Winter oceanographic conditions in the southwestern part of the Okhotsk Sea and their relation to sea ice. *J. Oceanogr.*, 57, 451–460.

Parkinson, C. L. (2019). A 40-y record reveals gradual Antarctic sea ice increases followed by decreases at rates far exceeding the rates seen in the Arctic. *Proceedings of the National Academy of Sciences of the United States of America*, 116, 14414–14423.

Rosenblum, E., and I. Eisenman, 2017, Sea ice trends in climate models only accurate in runs with biased global warming. *J. clim.* 30, 6265–6278.

Rudels, B., G. Bjork, J. Nilsson, P. Winsor, I. Lake, and C. Nohr, 2005: The interaction between water from the Arctic Ocean and the Nordic Seas north of Fram Strait and along the East Greenland Current: Results from the Arctic Ocean-02 Oden expedition. *J. Mar. Syst.*, 55, 1–30.

Rudels, B., M. Korhonen, U. Schauer, S. Pisarev, B. Rabe, and A. Wisotzki, 2015, Circulation and transformation of Atlantic water in the Eura-sian Basin and the contribution of the Fram Strait inflow branch to the Arctic Ocean heat budget, *Prog.Oceanogr.*, 132, 128–152.

Rudels, B., 2016, Arctic Ocean stability: The effects of local cooling, oceanic heat transport, freshwater input, and sea ice melt with special emphasis on the Nansen Basin, *J. Geophys. Res. Oceans*, 121, 4450–4473, doi:10.1002/ 2015JC011045.

Sagawa, G. (2007), Development of ice dynamic model that takes account of floe collision and its validation in numerical sea ice forecast in the Sea of Okhotsk, Ph.D. diss., Univ. of Tokyo, Tokyo.

Saiki, R., and Mitsudera, H., 2016, A Mechanism of Ice-Band Pattern Formation Caused by Resonant Interaction between Sea Ice and Internal Waves: A Theory, *J. phys. Oceanogra.*, 46(2), 583–600

Steele, M. J. H. Morison, and N. Untersteiner, 1989, The partition of air-ice-ocean momentum exchange as function of ice concentration, floe size and draft, *J. Geophys. Res.*, 94 (C9), 12,739–12,750.

Stroeve, J., M. M. Holland, W. Meier, T. Scambos, and M. Serreze, 2007, Arctic sea ice decline: Faster than forecast, *J. Geophys. Res. Lett.*, 34, L09501.

Sutherland, P., D., Dumont, 2018, Marginal Ice Zone Thickness and Extent due to Wave Radiation Stress, *J. Geophys. Res.*, 48, 1885–1901.

Swart, S., M. D. du Plessis, A. F. Thompson, L. C. Biddle, I. Giddy, T. Linders, M. Mohrmann, and S. A. Nicholson, 2020, Submesoscale fronts in the Antarctic marginal ice zone and their response to wind forcing, *J. Geophys. Res. Lett.*, 47.

Toyota, T., S. Takatsuji, and M. Nakayama, 2006, Characteristics of sea ice floe size distribution in the seasonal ice zone, *J. Geophys Res Lett*, 33, L02616.

Toyota, T., A.L. Kohout, and A.D. Fraser, 2016, Formation processes of sea ice floe size distribution in the interior pack and its relationship to the marginal ice zone off East Antarctica, *Deep − Sea Research II*, 131, 28-40.

Wadhams, P. 1983, A mechanism for the formation of ice edge bands, *J. Geophys. Res.*, 88 (C5), 2813–28118.

Wadhams, P. 2000, *Ice in the Ocean*, Gordon and Breach Science Publishers, 351 pp.

Wong, A. P. S., and S. C. Riser., 2011, Profiling float observations of upper ocean under sea ice off the Wilkes Land Coast of Antarctica *J. Phys. Oceanogra*,. 41, 1102–1115.

Figure Captions

Figure 1 (a) Satellite images of ice-band patterns on March 21, 2010, from Moderate-Resolution Imaging Spectroradiometer (MODIS) images by the National Aeronautics and Space Administration (NASA) [URL: http://lance-modis.eosdis.nasa.gov /imagery/subsets/?mosaic=Arctic]. Wind vectors (ms^{-1}) are derived from 10 m wind vectors of ERA-Interium (*Dee, D. P. et al.*, 2011) (b) Enlarged view in the red box of Fig. 1a shows ice bands. (c) Satellite images of ice-band patterns in the Eurasian Basin of the Arctic Sea on March 24, 2018, from MODIS [URL: http://lance-modis.eosdis.nasa.gov/imagery]. The domain of Fig. 1a is denoted by a red dashed box on Fig. 1c. (d) Enlarged view in the red box of Fig. 1c showing ice bands.

Figure 2 (a) Nomenclature and momentum balance on sea ice. (b) Stress applied to the sea surface at each point. $\boldsymbol{\tau}_{ai}$, $\boldsymbol{\tau}_{iw}$, and $\boldsymbol{\tau}_{aw}$ represent the the air–ice, ice–water, and air–water stresses, respectively. θ_a denotes the wind direction associated with both $\boldsymbol{\tau}_{ai}$ and $\boldsymbol{\tau}_{aw}$, while θ_i is the direction of $\boldsymbol{\tau}_{iw}$, and $\delta\theta$ is the turning angle between $\boldsymbol{\tau}_{ai}$

and $\boldsymbol{\tau}_{iw}$. A denotes the ice concentration.

Figure 3 (a) Dispersion relationship between the non-dimensional wave number $k^* = kL$ ($L = 1000$ m) and the non-dimensional frequency $\omega^* = \omega/f$. The three curves are derived from the first, second, and third mode dispersion relationships, respectively. The numbers near the curves denote the baroclinic mode numbers of the internal waves. The red line denotes $\overline{U}_i^{\,*}$, representing a band propagation speed on $k^* - \omega^*$ plane. The dashed line corresponds to the inertial frequency on the $k^* - \omega^*$ plane. The three blue points with down arrows indicate resonance points when the coupling between sea ice and internal waves occurs (e.g. *Saiki and Mitsudera*, 2016). (b) Relationship between the non-dimensional ice-band propagation speed $\overline{U}_i^* = \overline{U}_i/fL$ and the non-dimensional band spacing $\lambda^* = \lambda/L$. The number adjacent to each curve coincides with each baroclinic mode numbers of the internal waves.

Figure 4 Initial stratification of the exponential type where a potential density profile is given by $-20\exp\{-0.01(z+200)\} + 1026.72$.

Figure 5 Relationship between the wind direction and non-dimensional theoretical growth rate.

Figure 6 Ice-band formation for an ice-edge case when a homogeneous wind $(U_a, V_a) = (7.5\ \mathrm{ms}^{-1}, 7.5\ \mathrm{ms}^{-1})$ is imposed, where U_a denotes the x-component of the wind speed, and V_a denotes the y-component. The color shade denotes the sea-ice concentration. (a) Initial state of this numerical experiment. White vectors represent wind vectors. A homogeneous wind is given over the whole domain. (b) Ice bands 6.75 days after the initial state of Fig. 6a.

Figure 7 Sea-ice concentration and vertical section of the vertical velocity in the ice-band pattern propagation direction. (a), (c), and (e) represent the sea-ice concentration after 3 days, 5 days, 6.75 days from the initial state, respectively. (b), (d), and (f) represent the vertical flows under ice bands after 3 days, 5 days, and 6.75 days from the initial state, respectively. The color shade denotes the vertical-flow speed (ms^{-1}).

Figure 8 (a) $(U_a, V_a) = (6.0\,\mathrm{ms}^{-1}, 6.0\,\mathrm{ms}^{-1})$ on day 8, and (b) $(U_a, V_a) = (9.0\,\mathrm{ms}^{-1}, 9.0\,\mathrm{ms}^{-1})$ on day 6.75. The vertical axis denotes the sea-ice concentration, and the horizontal axis denotes the distance of band pattern propagation.

Figure 9 Relationship between the band pattern propagation speed $\overline{U}_i$ and the band spacing λ. The solid lines denote the theoretical curves, and the square points denote the numerical results. Numbers adjacent to the theoretical curves denote the baroclinic modes.

Figure 10 Experiments with various wind directions, in which (a) $\theta_a = \pi/2$, (b) $\theta_a = \pi/4$, (c) $\theta_a = 0$, and (d) $\theta_a = -\pi/4$, are shown. (e) Numerical results of the growth rate. The lateral axis denotes the wind direction with respect to the ice edge. The vertical axis denotes the growth rate (day^{-1}) defined by the growth of the vertical-flow amplitude between day 3 and day 4 per unit volume. Marker ● denotes cases in which exponential growth is well defined on day 4. Marker $\times$ denotes cases in which exponential growths were not clear.

Figure 11 Ice-band pattern formation over a deep ocean. (a) Initial profile of density up to 400 m. Density below 400 m increases with depth with $N_B = 0.0045$ s^{-1}. (b) Sea-ice concentration (upper panel) and vertical flows under ice bands (lower panel) 2 days after the initial state. (c) Same as (b) but for 5 days after the initial state.

Figure 12 Ice-band pattern formation from a homogeneous initial condition. (a) Initial condition. The random ice concentration from 0 to 1 is given as the white noise all over this domain. White vectors represent the homogeneous wind, given as $(U_a, V_a) = (7.5 \text{ ms}^{-1}, 7.5 \text{ ms}^{-1})$. (b) Ice-band patterns 7 days after the initial state. The color shade denotes a parameter defined by the product o the sea-ice concentration and the ice thickness. (c) Vertical-flow section at the black line of Fig. 12b. The color shade denotes the vertical-flow speed (ms^{-1}).

Figure 13 Plume-like ice-band pattern in the MIZ. (a) Initial state. The MIZ is set at the left side of the domain. The white vectors denote the wind vectors. The color shade denotes the sea-ice concentration. (b) Ice-band pattern formation on day 10.

Figure 14 Example of selection of five bands in a target area.

Figure 15 (a) Relationship between non-dimensional wind speed and non-dimensional band spacing. "obs.(ber)" denotes the results of the Bering Sea observations (redrawn from *Muench and Charnell*, 1977, Fig. 5). "obs.(okh)" denotes the results of the Okhotsk Sea observations. "obs.(grl)" denotes the results of the East Greenland Current observations. The solid line denotes $\lambda_{max} = 2\pi\overline{U}_i/f$. The error bar denotes the standard deviation. Note that the scale of L is 10 km, U_i is 2.5% of the 10 m wind and f is 1.12×10^{-4} s^{-1}. (b) Initial density profile of the numerical experiments in Fig. 15a, denoted by "num.(ber)", which represents a typical profile of the winter Bering Sea (e.g. *Muench et al.*, 1983, Fig. 5). The potential density profile is given by $0.1 \tanh\{0.03(z-50)\} + 1026.105$, with z denoting the depth.

Figure 16 Non-dimensional dispersion relationship. The three curves represent the theoretical dispersion relationships of the inertia-gravity internal waves of the 2nd, 3rd, and 4th mode, respectively, where the density profile of Fig. 15b is used. The wave number in the horizontal axis is scaled by $L = 1$ km, whereas the frequency in the vertical axis is scaled by U_i/L where U_i is 2.5% of the 10 m wind. "obs.(okh)" denotes the results of the Okhotsk Sea observations. "obs.(grl)" denotes the results of the East Greenland Current observations. "obs.(ros)" denotes the results of the Ross Sea observations. "i.f." denotes the inertial frequency.

Figure 17 (a) Initial stratification to calculate the baroclinic phase speeds. The blue profile is used to calculate the theoretical band spacings in winter shown in (b), while the red profile is for band spacings in spring shown in (c). (b) Relationship between wind speed and band spacing in the Antarctic Ocean in the winter season (Aug., Sep.), and (c) spring season (Oct., Nov., Dec.)(redrawn from *Ishida and Ohshima*, 2009). Dots denote observations from satellites. Solid lines denote solutions for the blue profile in (a). Numbers on the curves in (b) and (c) denote the mode numbers. The black dashed line denotes the $\lambda - \overline{U}_i$ relationship associated with the inertial frequency f. Resonance may occur in the shaded part according to the theory. The baroclinic phase speeds in the winter case (blue curves) are $c_2 = 0.119$ ms^{-1}, $c_3 = 0.070$ ms^{-1}, $c_4 = 0.050$ ms^{-1}, $c_5 = 0.039$ ms^{-1}, and $c_6 = 0.032$ ms^{-1}, where the subscripts denote the mode numbers, respectively. The baroclinic phase speeds in the spring case (red curves) are $c_3 = 0.209$ ms^{-1}, $c_4 = 0.156$ ms^{-1}, $c_5 = 0.125$ ms^{-1}, $c_6 = 0.104$ ms^{-1}, and $c_7 = 0.089$ ms^{-1}. The white dashed line in (b) indicates the maximum band spacing λ_{Emax} derived from the baroclinic phase speeds in winter (spring), which is evaluated from the lowest possible mode that can be resonant, while that in (c) indicates λ_{Emax} in spring.

Figure 18 Ice-band pattern formation in which mean ice concentration $\overline{A}$ is 0.9. (a) Ice concentration along the black arrow of Fig. 18b, (b) horizontal distribution of initial ice concentration, and (c) ice-band patterns after 10 days from the initial state of (b). White arrows denotes the wind vectors.

Figure 19 Ice-band pattern distribution with respect to wind direction and ice concentration. (a) Typical types of ice-band pattern. × denotes a pattern without band formation. ○ denotes a pattern dominated by the effect of initial random ice concentration. △ denotes a pattern representing band formation due to initial random ice concentration in the interior ice field along with an effect of ice-edge without band formation. □ denotes a pattern representing band formation due to both the effect of ice edge and the effect of the initial random ice concentration. ◇ denotes a pattern dominated by the effect of ice edge with band formation. White arrows in the patterns denote wind vectors. (b) Ice-band pattern type distribution with respect to wind direction θ_a and ice concentration $\overline{A}$.

Figure 20 Effect of ice thickness on the ice-band pattern formation. Ice thickness of (a) 0.1 m and (b) 1.0 m. Results on day 7 are shown. The color shade denotes the sea-ice concentration.

Figure 21 Relationship between ice-water drag coefficient C_{Diw} and band spacing λ. ● denotes numerical results. ○ denotes cases that give two numerical values for a single drag coefficient. Three curves in this figure denote theoretical results of 1st, 2nd, and 3rd modes, respectively, evaluated by the band propagation speed with varying C_{Diw}.

Figure 22 Experiments with variable wind intensities. The wind intensity varied with (a) 2-day, (b) 4-day, and (c) 8-day periods. The upper panels display the wind intensity with time, while the lower panels display numerical results on day 7. The color shade in the lower panels denotes the sea-ice concentration.

Figure 23 Relationship between latitude (Coriolis parameter) and band spacing. ● denote the numerical results. Dashed curve indicates the theoretical results.

Figure 24 Non-rotational experiment. (a) Initial sea-ice concentration. (b) Sea-ice concentration 4 days after the initial state. (c) Vertical section of the velocity field. The vector unit is ms^{-1}. The vertical velocity is multiplied by 1000 to draw the vectors. The color shade denotes the vertical velocity.

Captions for tables

Table 1: Model Parameters

Table 2: Basic Setting of Contorol Experiment

Table 3: Varying parameters from Control Experiment

Table 1: Model Parameters

Name	Description	Value
dt_{ext}	time step in external mode	15 sec
dt_{int}	time step in internal mode	30 sec
dt_{ice}	time step in ice thermodynamic model	15 sec
C_{Dai}	air-ice drag coefficient	3.0×10^{-3}
C_{Daw}	air-water drag coefficient	1.5×10^{-3}
C_{Diw}	ice-water drag coefficient	6.0×10^{-3}
c_h	ice-water heat transfer coefficient	5.0×10^{-3}
ρ_a	density of the air	1.247 kg m^{-3}
ρ_w	density of the ocean	1025.9 kg m^{-3}
ρ_i	density of sea ice	910.0 kg m^{-3}
L_i	melting latent heat of sea ice	3.3×10^{-5} J kg^{-1}

Table 2: Basic Setting of Contorol Experiment

Description	Value
ocean model	
numerical domain	160 km × 220 km
horizontal resolution	250 m × 250 m
vertical resolution	31 layers
sea depth	150 m
salinity	32.0 – 33.5 psu
temperature	-1.0 – 0.0 °C
Colioris parameter	$2 \times 0.729 \times 10^{-4} \times \sin 50^{\circ}$ s^{-1}
ice model	
initial sea-ice area	0.25 × 160 km × 220 km
sea-ice concentration	0.5
ice thickness	0.5 m
homogeneous wind forcing	
wind vector	$(U_a, V_a) = (7.5 \text{ ms}^{-1}, 7.5 \text{ ms}^{-1})$

Table 3: Varying Parameters from Control Experiment

Section	Varying Parameter	Figure of each results
3.1.1	(contorol experiment)	Fig. 6, Fig. 7
3.1.2	wind speed $\boldsymbol{U}_a$ (ms^{-1})	Fig. 8, Fig. 9
3.1.3	wind direction θ_a (rad)	Fig. 10
3.1.4	ocean depth (m), total layers, initial stratification	Fig. 11
3.2.1	initial mean ice concentration $\overline{A}$	Fig. 12
3.2.2	domain size (km^2), initial mean ice concentration $\overline{A}$	Fig. 13
5.1	initial mean ice concentration $\overline{A}$	Fig. 18, Fig. 19
5.2	initial ice thickness$d$ (m)	Fig. 20
5.3	ice–water drag coefficient C_{Diw}	Fig. 21
5.4	wind intensity $\boldsymbol{U}_a$ (ms^{-1})	Fig. 22
5.5	Colioris parameter f (s^{-1})	Fig. 23, Fig. 24

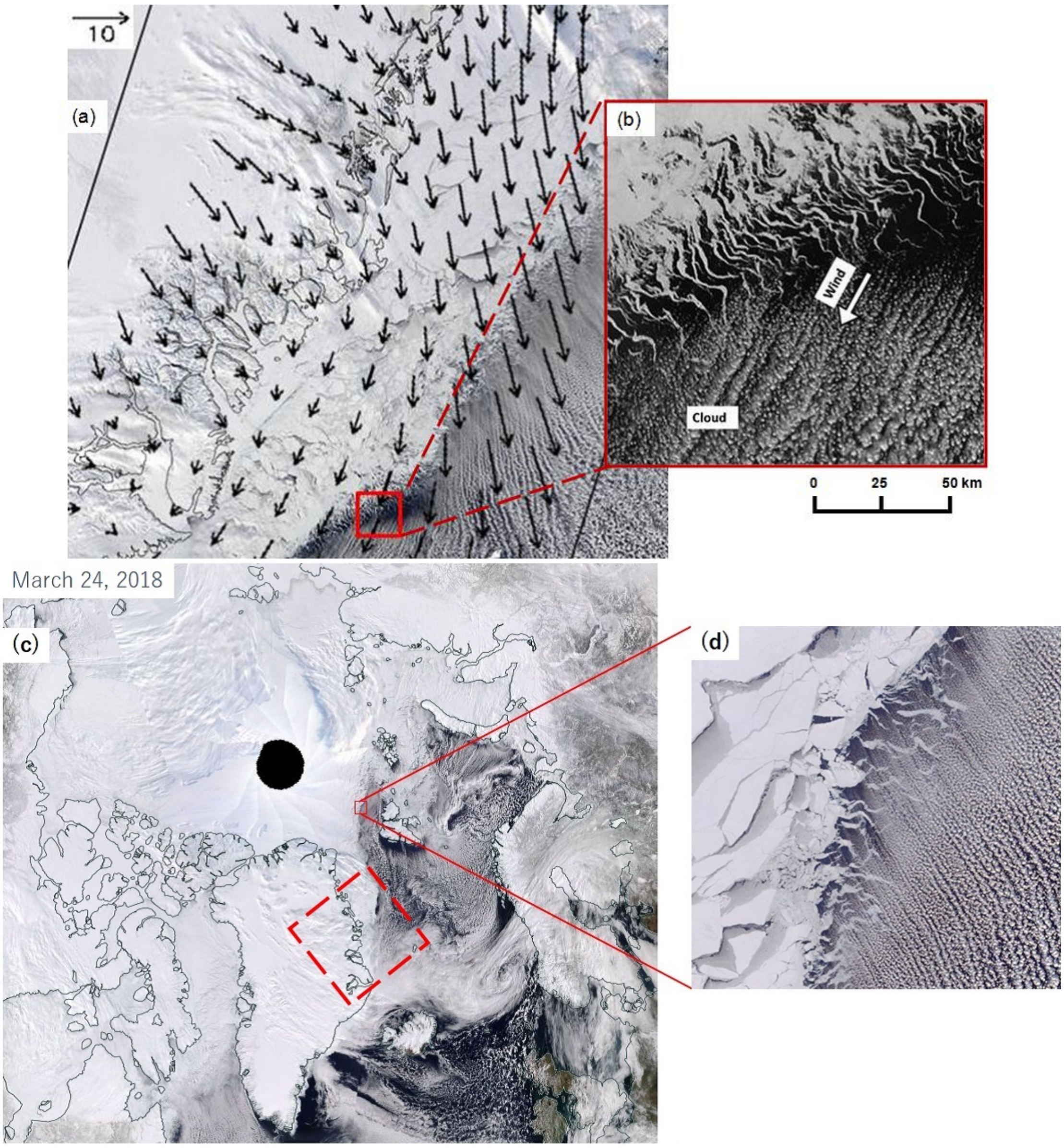

Figure 1: (a) Satellite images of ice-band patterns on March 21, 2010, from Moderate-Resolution Imaging Spectroradiometer (MODIS) images by the National Aeronautics and Space Administration (NASA) [URL: http://lance-modis.eosdis.nasa.gov/imagery/subsets/?mosaic=Arctic]. Wind vectors (ms^{-1}) are derived from 10 m wind vectors of ERA-Interium (*Dee, D. P. et al.*, 2011) (b) Enlarged view in the red box of Fig. 1a shows ice bands. (c) Satellite images of ice-band patterns in the Eurasian Basin of the Arctic Sea on March 24, 2018, from MODIS [URL: http://lance-modis.eosdis.nasa.gov /imagery]. The domain of Fig. 1a is denoted by a red dashed box on Fig. 1c. (d) Enlarged view in the red box of Fig. 1c showing ice bands.

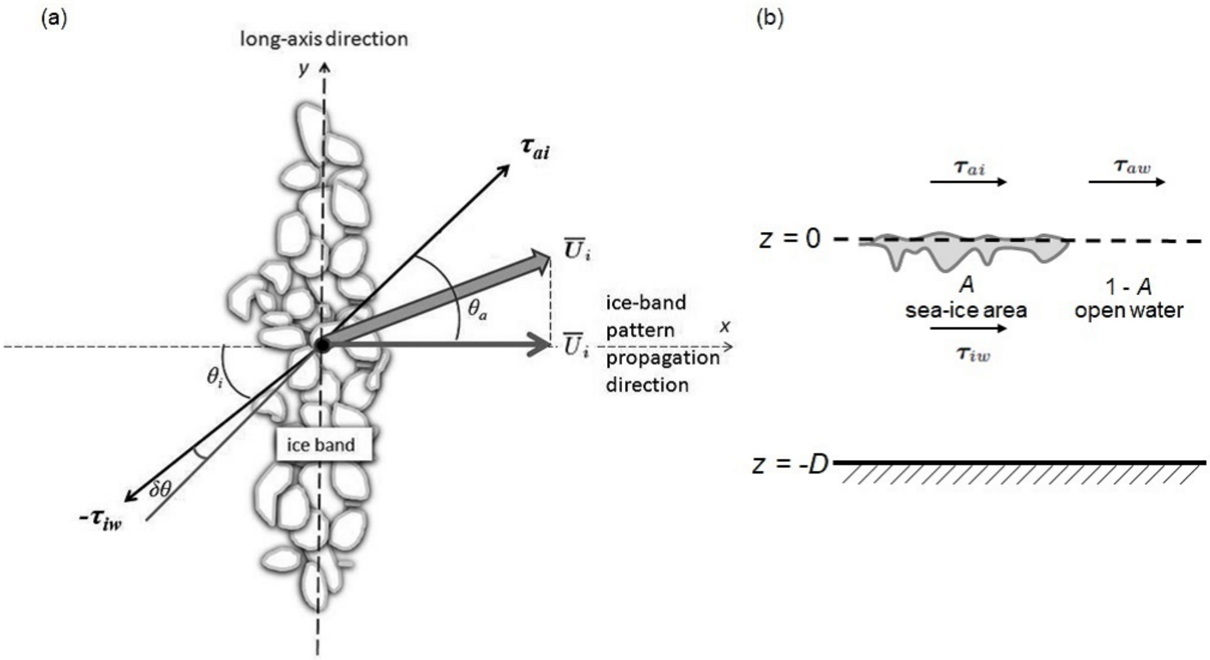

Figure 2: (a) Nomenclature and momentum balance on sea ice. (b) Stress applied to the sea surface at each point. $\boldsymbol{\tau}_{ai}$, $\boldsymbol{\tau}_{iw}$, and $\boldsymbol{\tau}_{aw}$ represent the the air–ice, ice–water, and air–water stresses, respectively. θ_a denotes the wind direction associated with both $\boldsymbol{\tau}_{ai}$ and $\boldsymbol{\tau}_{aw}$, while θ_i is the direction of $\boldsymbol{\tau}_{iw}$, and $\delta\theta$ is the turning angle between $\boldsymbol{\tau}_{ai}$ and $\boldsymbol{\tau}_{iw}$. A denotes the ice concentration.

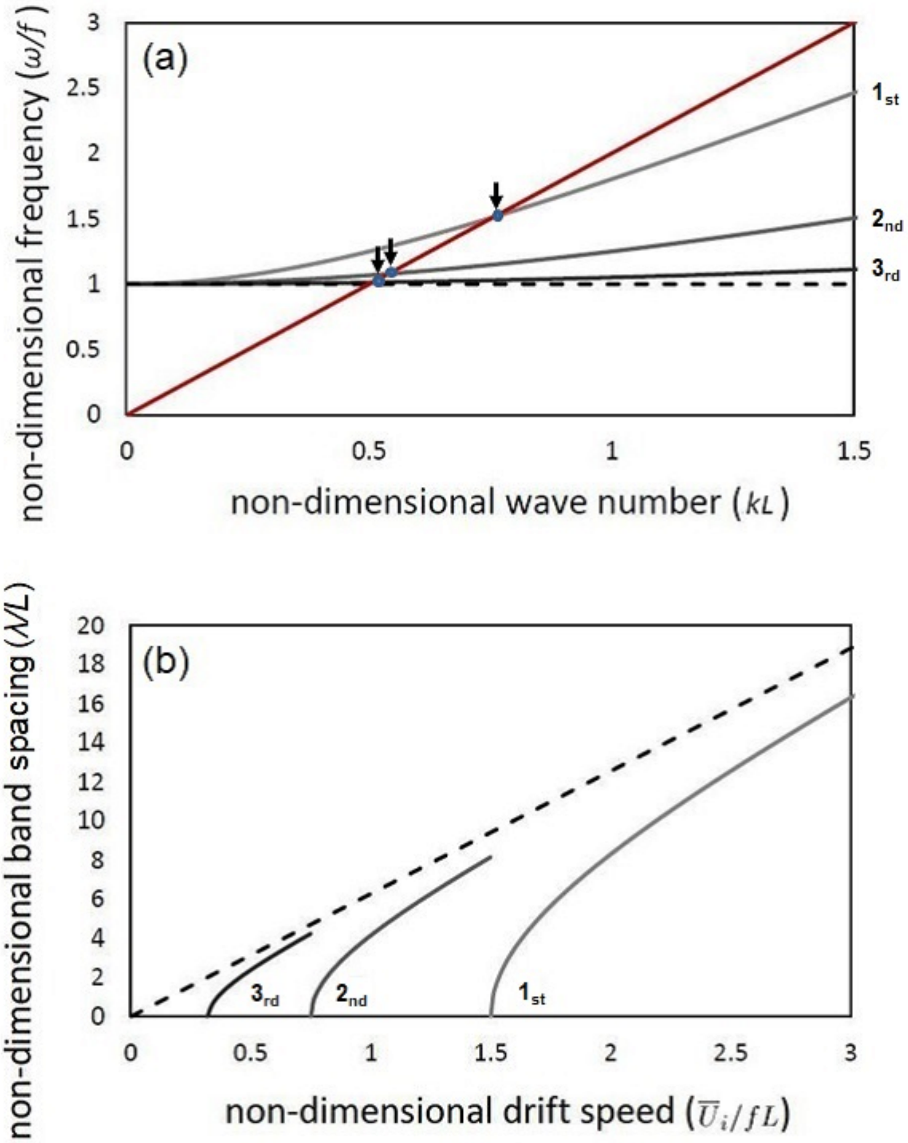

Figure 3: (a) Dispersion relationship between the non-dimensional wave number $k^* = kL$ ($L =$ 1000 m) and the non-dimensional frequency $\omega^* = \omega/f$. The three curves are derived from the first, second, and third mode dispersion relationships, respectively. The numbers near the curves denote the baroclinic mode numbers of the internal waves. The red line denotes $\overline{U}_i{}^*$, representing a band propagation speed on $k^* - \omega^*$ plane. The dashed line corresponds to the inertial frequency on the $k^* - \omega^*$ plane. The three blue points with down arrows indicate resonance points when the coupling between sea ice and internal waves occurs (e.g. *Saiki and Mitsudera*, 2016). (b) Relationship between the non-dimensional ice-band propagation speed $\overline{U}_i^* = \overline{U}_i/fL$ and the non-dimensional band spacing $\lambda^* = \lambda/L$. The number adjacent to each curve coincides with each baroclinic mode numbers of the internal waves.

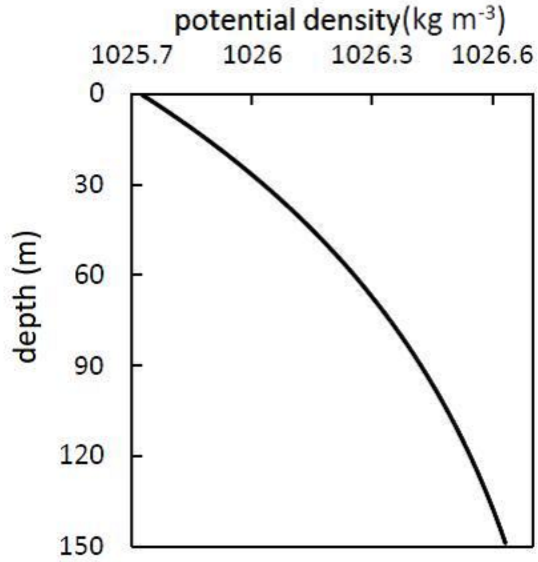

Figure 4: Initial stratification of the exponential type where a potential density profile is given by $-20\exp\{-0.01(z+200)\}+1026.72$.

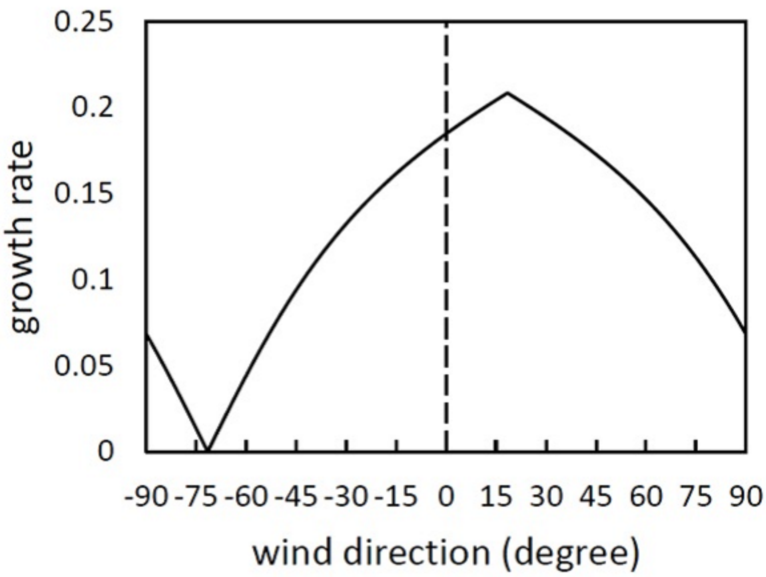

Figure 5: Relationship between the wind direction and non-dimensional theoretical growth rate.

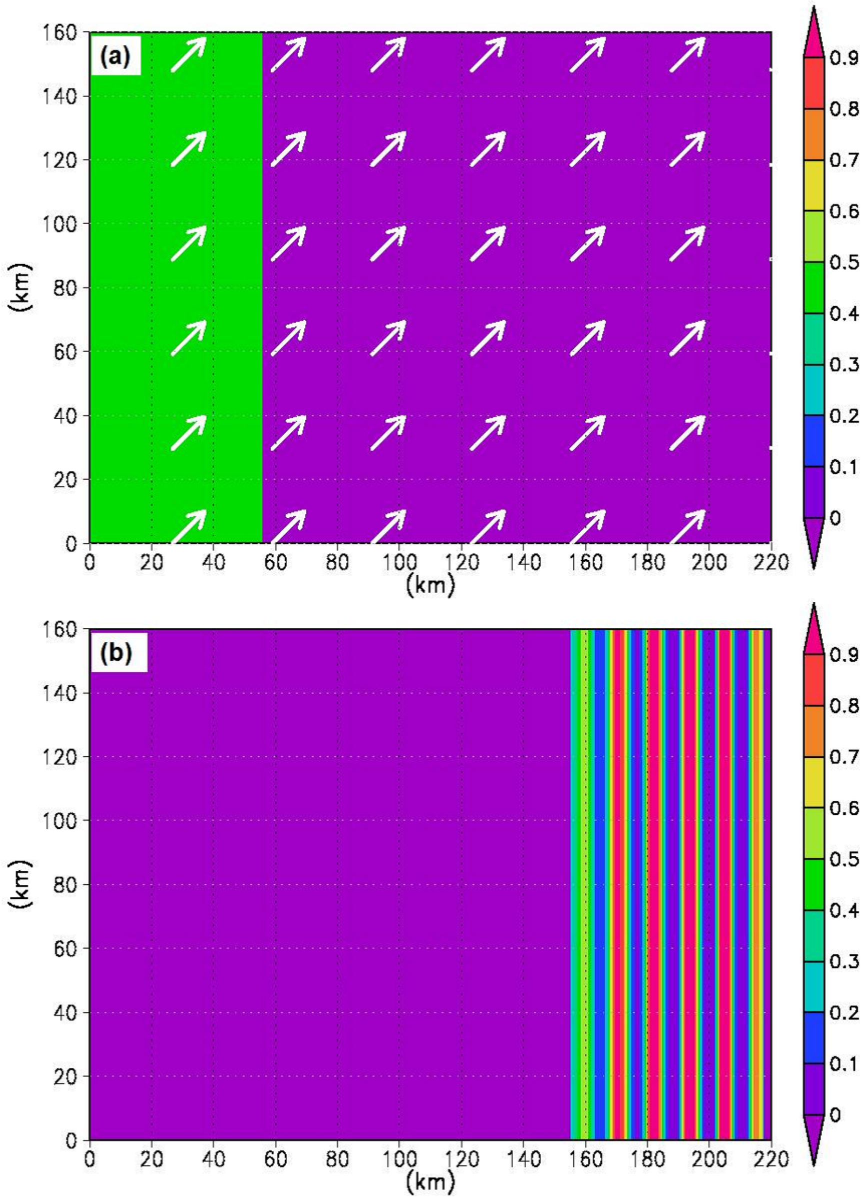

Figure 6: Ice-band formation for an ice-edge case when a homogeneous wind $(U_a, V_a) = (7.5\ \mathrm{ms}^{-1}, 7.5\ \mathrm{ms}^{-1})$ is imposed, where U_a denotes the x-component of the wind speed, and V_a denotes the y-component. The color shade denotes the sea-ice concentration. (a) Initial state of this numerical experiment. White vectors represent wind vectors. A homogeneous wind is given over the whole domain. (b) Ice bands 6.75 days after the initial state of Fig. 6a.

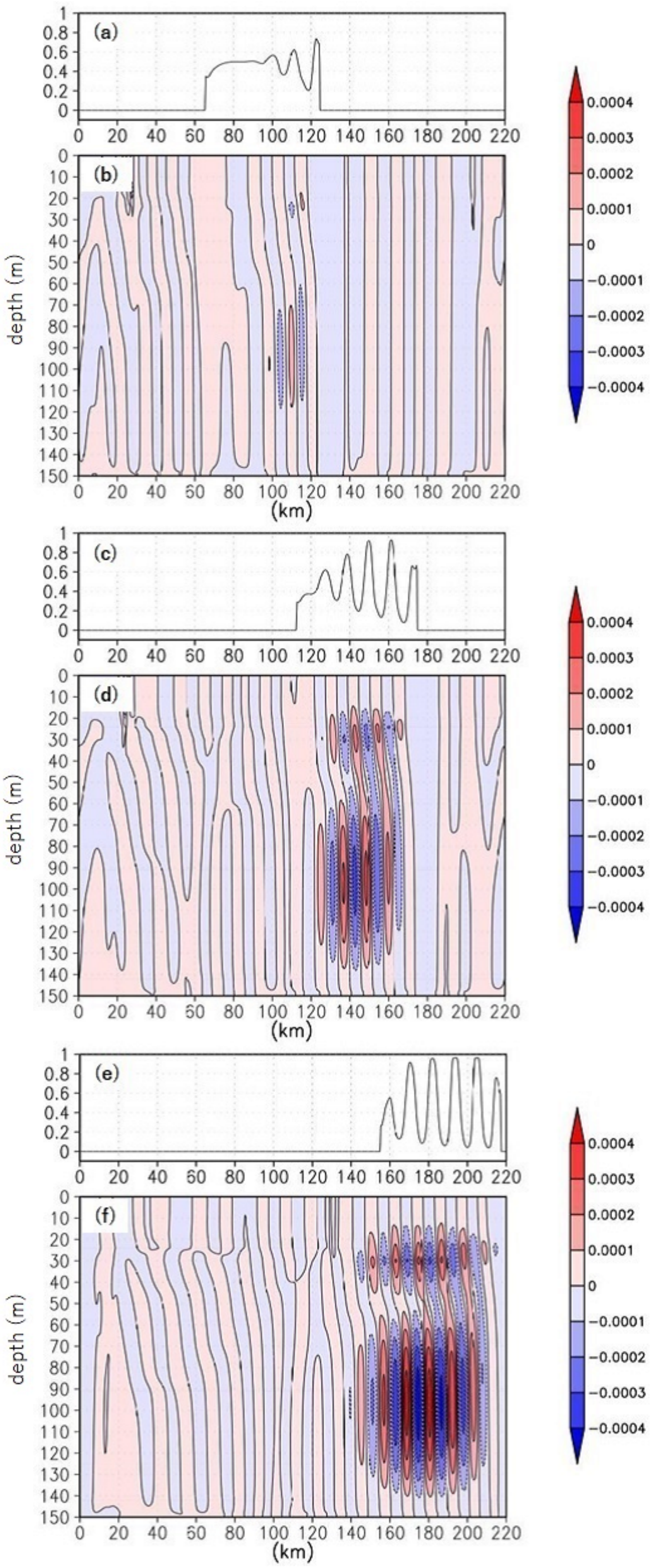

Figure 7: Sea-ice concentration and vertical section of the vertical velocity in the ice-band pattern propagation direction. (a), (c), and (e) represent the sea-ice concentration after 3 days, 5 days, 6.75 days from the initial state, respectively. (b), (d), and (f) represent the vertical flows under ice bands after 3 days, 5 days, and 6.75 days from the initial state, respectively. The color shade denotes the vertical-flow speed (ms^{-1}).

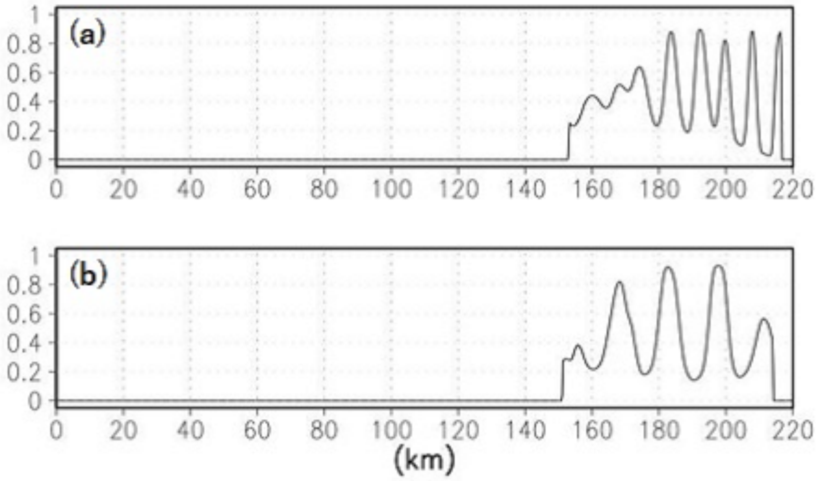

Figure 8: (a) $(U_a, V_a) = (6.0 \text{ ms}^{-1}, 6.0 \text{ ms}^{-1})$ on day 8, and (b) $(U_a, V_a) = (9.0 \text{ ms}^{-1}, 9.0 \text{ ms}^{-1})$ on day 6.75. The vertical axis denotes the sea-ice concentration, and the horizontal axis denotes the distance of band pattern propagation.

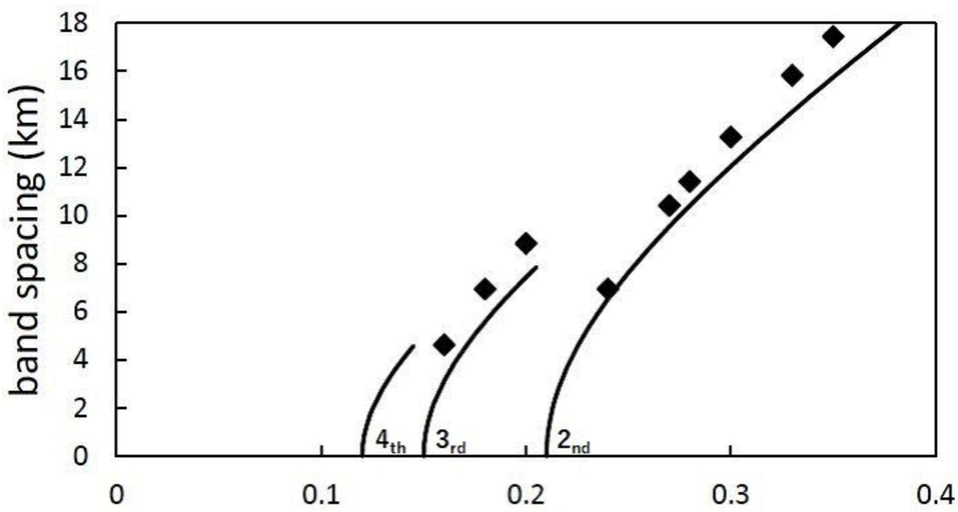

Figure 9: Relationship between the band pattern propagation speed $\overline{U}_i$ and the band spacing λ. The solid lines denote the theoretical curves, and the square points denote the numerical results. Numbers adjacent to the theoretical curves denote the baroclinic modes.

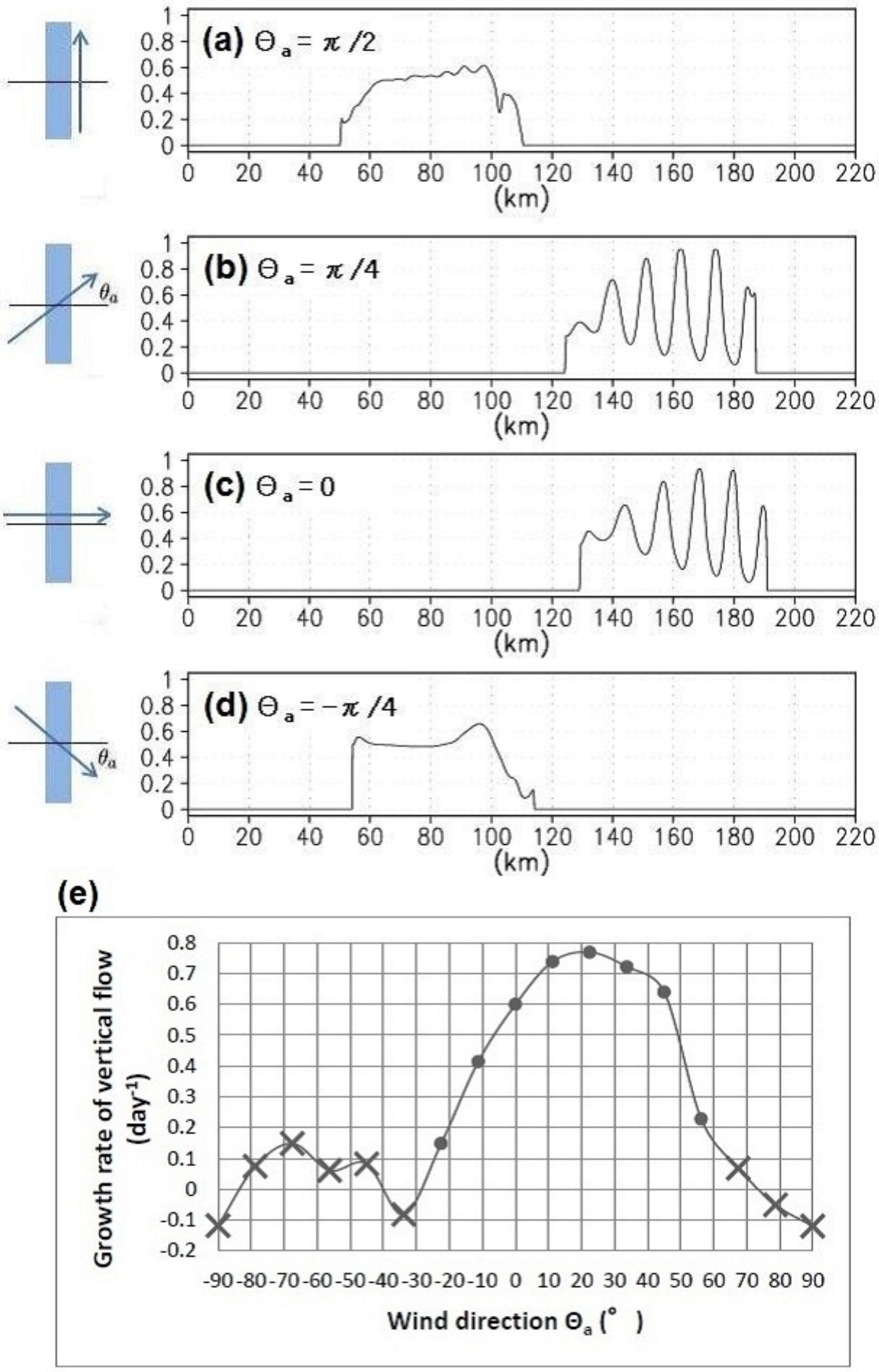

Figure 10: Experiments with various wind directions, in which (a) $\theta_a = \pi/2$, (b) $\theta_a = \pi/4$, (c) $\theta_a = 0$, and (d) $\theta_a = -\pi/4$, are shown. (e) Numerical results of the growth rate. The lateral axis denotes the wind direction with respect to the ice edge. The vertical axis denotes the growth rate (day^{-1}) defined by the growth of the vertical-flow amplitude between day 3 and day 4 per unit volume. Marker ● denotes cases in which exponential growth is well defined on day 4. Marker × denotes cases in which exponential growths were not clear.

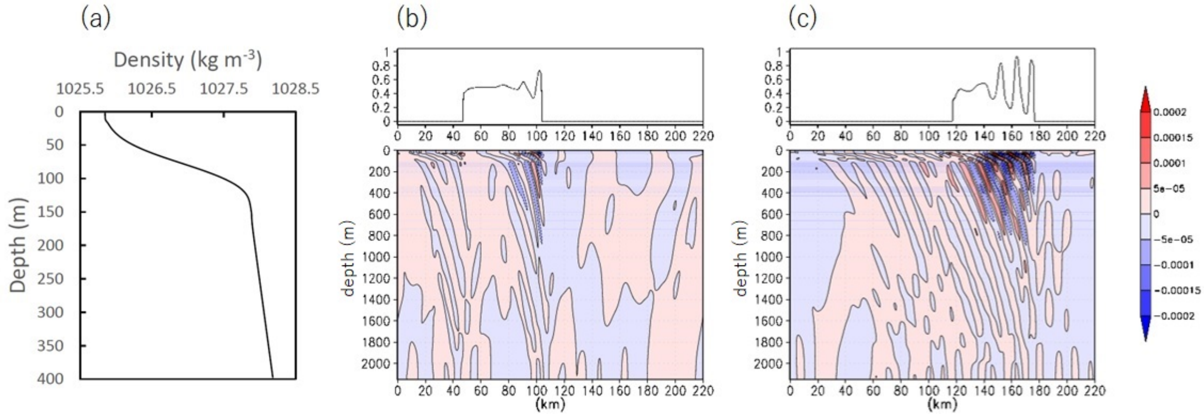

Figure 11: Ice-band pattern formation over a deep ocean. (a) Initial profile of density up to 400 m. Density below 400 m increases with depth with $N_B = 0.0045\ \mathrm{s}^{-1}$. (b) Sea-ice concentration (upper panel) and vertical flows under ice bands (lower panel) 2 days after the initial state. (c) Same as (b) but for 5 days after the initial state.

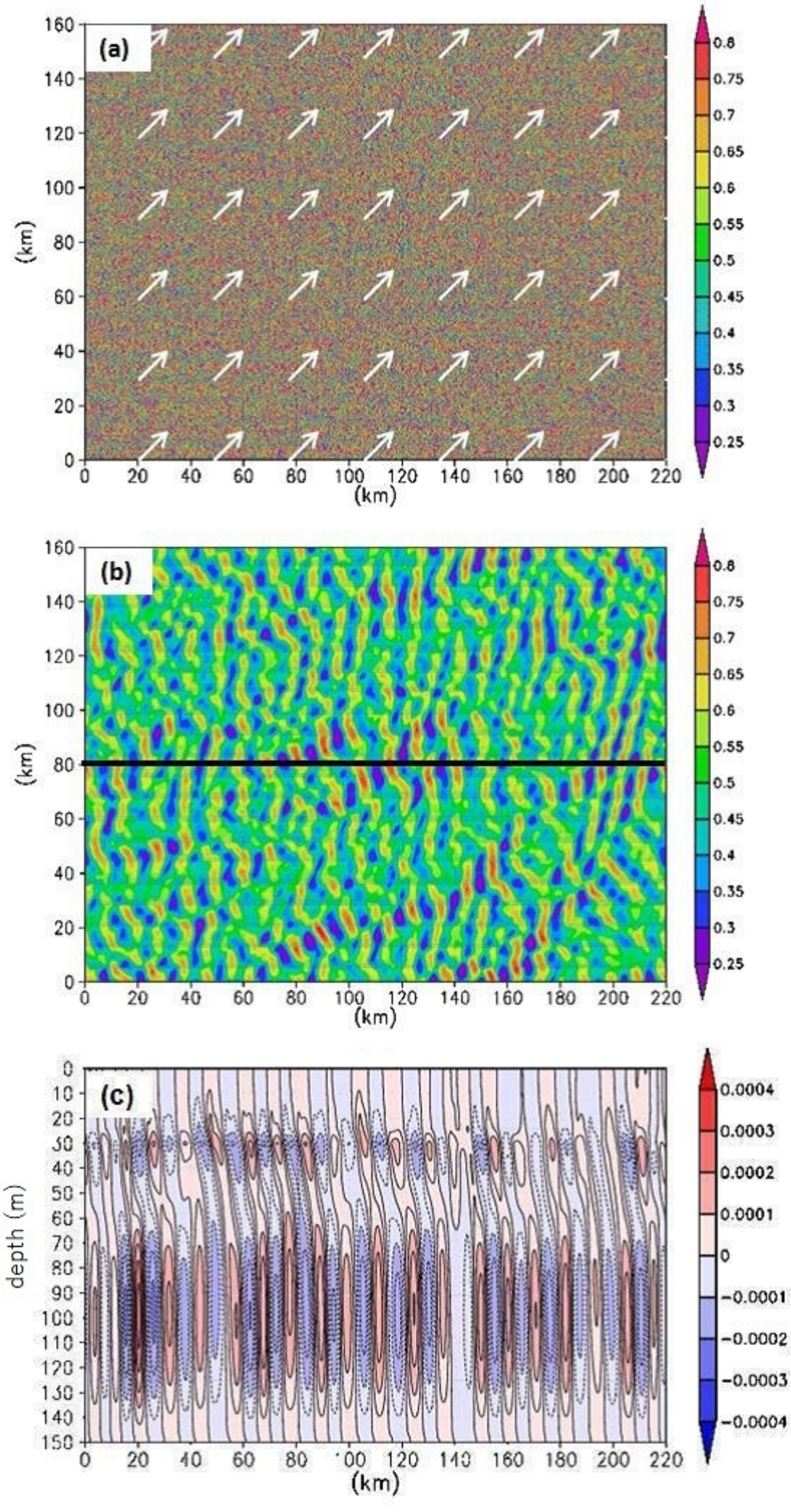

Figure 12: Ice-band pattern formation from a homogeneous initial condition. (a) Initial condition. The random ice concentration from 0 to 1 is given as the white noise all over this domain. White vectors represent the homogeneous wind, given as $(U_a, V_a) = (7.5\ \mathrm{ms}^{-1}, 7.5\ \mathrm{ms}^{-1})$. (b) Ice-band patterns 7 days after the initial state. The color shade denotes a parameter defined by the product o the sea-ice concentration and the ice thickness. (c) Vertical-flow section at the black line of Fig. 12b. The color shade denotes the vertical-flow speed (ms^{-1}).

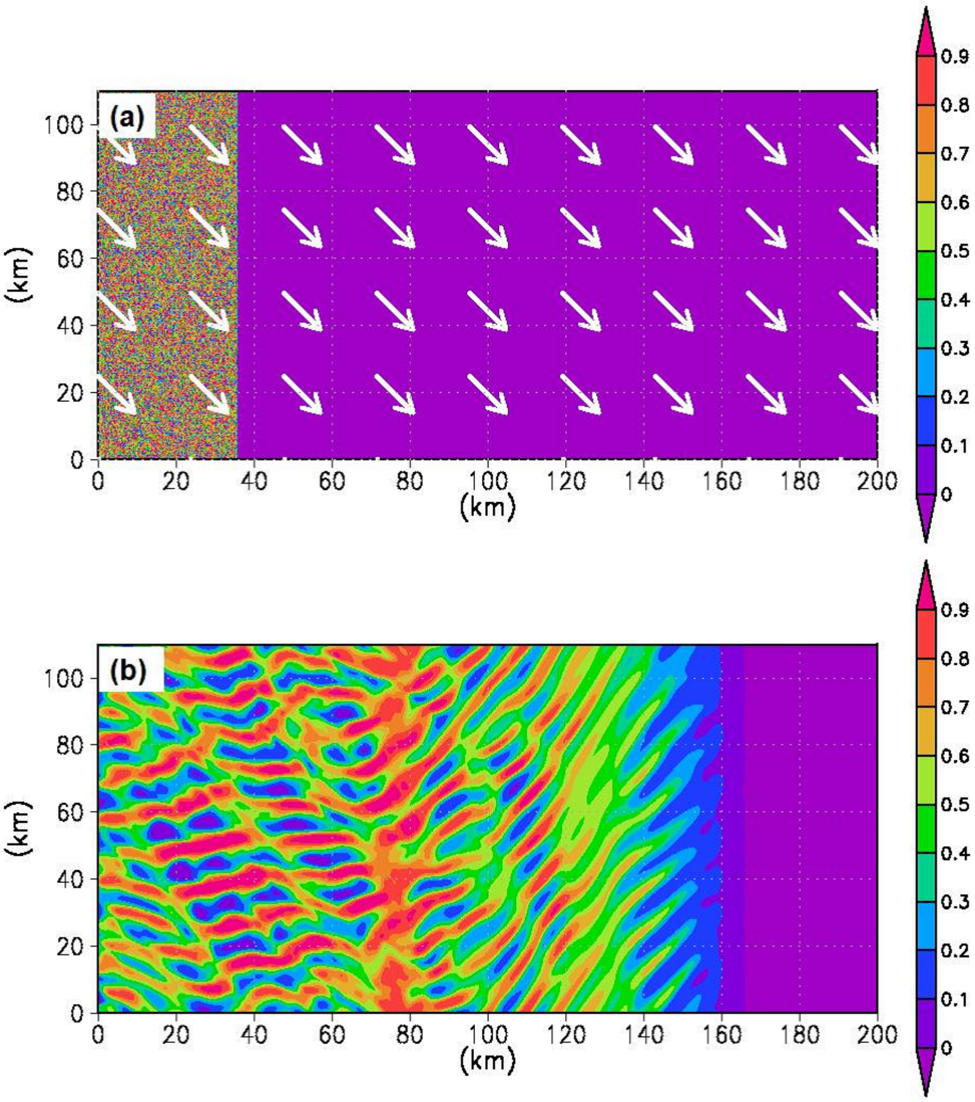

Figure 13: Plume-like ice-band pattern in the MIZ. (a) Initial state. The MIZ is set at the left side of the domain. The white vectors denote the wind vectors. The color shade denotes the sea-ice concentration. (b) Ice-band pattern formation on day 10.

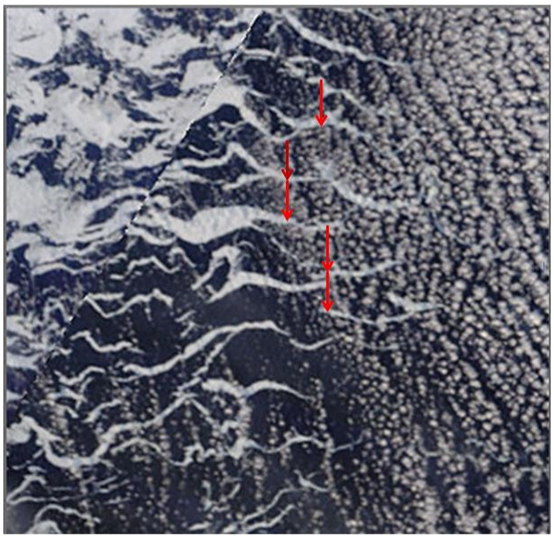

Figure 14: Example of selection of five bands in a target area.

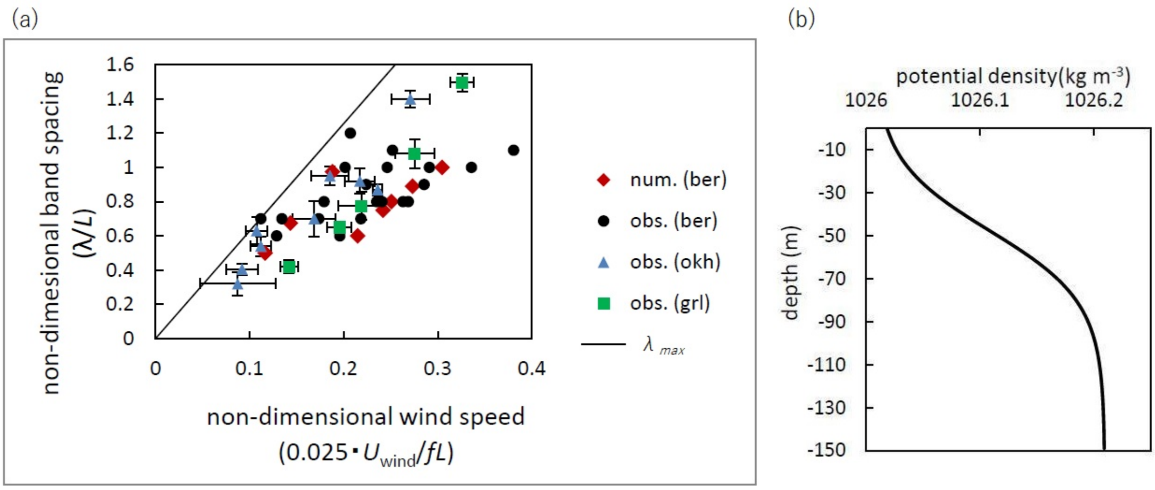

Figure 15: (a) Relationship between non-dimensional wind speed and non-dimensional band spacing. "obs.(ber)" denotes the results of the Bering Sea observations (redrawn from *Muench and Charnell*, 1977, Fig. 5). "obs.(okh)" denotes the results of the Okhotsk Sea observations. "obs.(grl)" denotes the results of the East Greenland Current observations. The solid line denotes $\lambda_{max} = 2\pi\overline{U}_i/f$. The error bar denotes the standard deviation. Note that the scale of L is 10 km, U_i is 2.5% of the 10 m wind and f is 1.12×10^{-4} s^{-1}. (b) Initial density profile of the numerical experiments in Fig. 15a, denoted by "num.(ber)", which represents a typical profile of the winter Bering Sea (e.g. *Muench et al.*, 1983, Fig. 5). The potential density profile is given by $0.1 \tanh\{0.03(z - 50)\} + 1026.105$, with z denoting the depth.

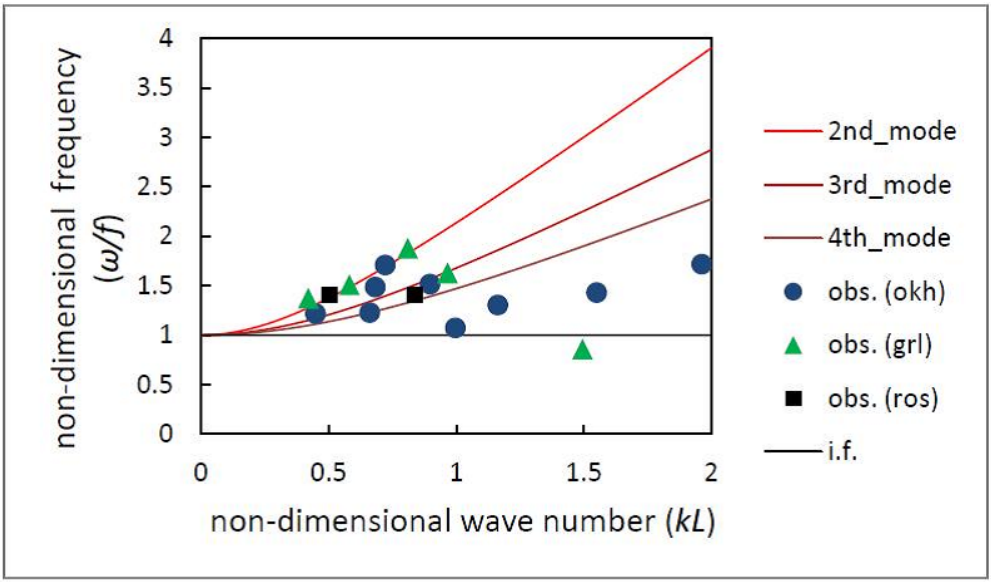

Figure 16: Non-dimensional dispersion relationship. The three curves represent the theoretical dispersion relationships of the inertia-gravity internal waves of the 2nd, 3rd, and 4th mode, respectively, where the density profile of Fig. 15b is used. The wave number in the horizontal axis is scaled by $L = 1$ km, whereas the frequency in the vertical axis is scaled by U_i/L where U_i is 2.5% of the 10 m wind. "obs.(okh)" denotes the results of the Okhotsk Sea observations. "obs.(grl)" denotes the results of the East Greenland Current observations. "obs.(ros)" denotes the results of the Ross Sea observations. "i.f." denotes the inertial frequency.

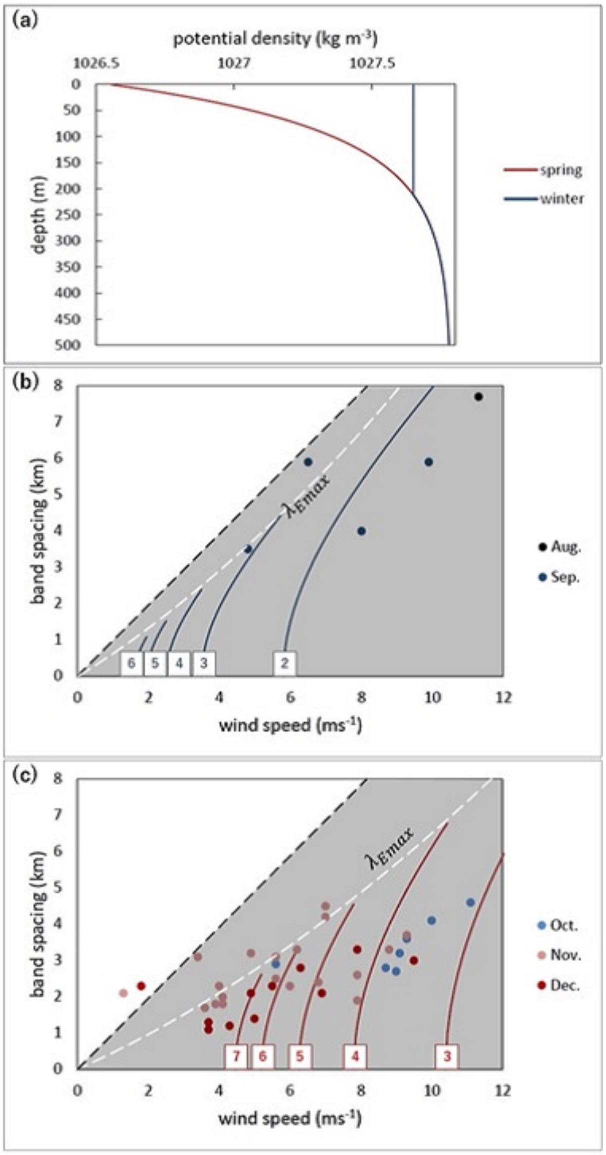

Figure 17: (a) Initial stratification to calculate the baroclinic phase speeds. The blue profile is used to calculate the theoretical band spacings in winter shown in (b), while the red profile is for band spacings in spring shown in (c). (b) Relationship between wind speed and band spacing in the Antarctic Ocean in the winter season (Aug., Sep.), and (c) spring season (Oct., Nov., Dec.)(redrawn from *Ishida and Ohshima*, 2009). Dots denote observations from satellites. Solid lines denote solutions for the blue profile in (a). Numbers on the curves in (b) and (c) denote the mode numbers. The black dashed line denotes the $\lambda - \overline{U}_i$ relationship associated with the inertial frequency f. Resonance may occur in the shaded part according to the theory. The baroclinic phase speeds in the winter case (blue curves) are $c_2 = 0.119$ ms^{-1}, $c_3 = 0.070$ ms^{-1}, $c_4 = 0.050$ ms^{-1}, $c_5 = 0.039$ ms^{-1}, and $c_6 = 0.032$ ms^{-1}, where the subscripts denote the mode numbers, respectively. The baroclinic phase speeds in the spring case (red curves) are $c_3 = 0.209$ ms^{-1}, $c_4 = 0.156$ ms^{-1}, $c_5 = 0.125$ ms^{-1}, $c_6 = 0.104$ ms^{-1}, and $c_7 = 0.089$ ms^{-1}. The white dashed line in (b) indicates the maximum band spacing λ_{Emax} derived from the baroclinic phase speeds in winter (spring), which is evaluated from the lowest possible mode that can be resonant, while that in (c) indicates λ_{Emax} in spring .

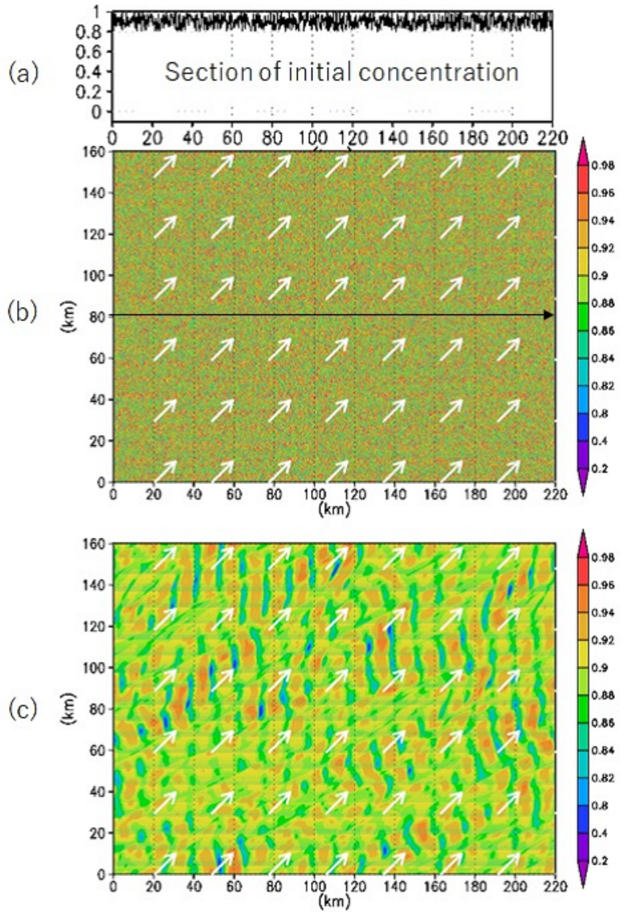

Figure 18: Ice-band pattern formation in which mean ice concentration $\overline{A}$ is 0.9. (a) Ice concentration along the black arrow of Fig. 18b, (b) horizontal distribution of initial ice concentration, and (c) ice-band patterns after 10 days from the initial state of (b). White arrows denotes the wind vectors.

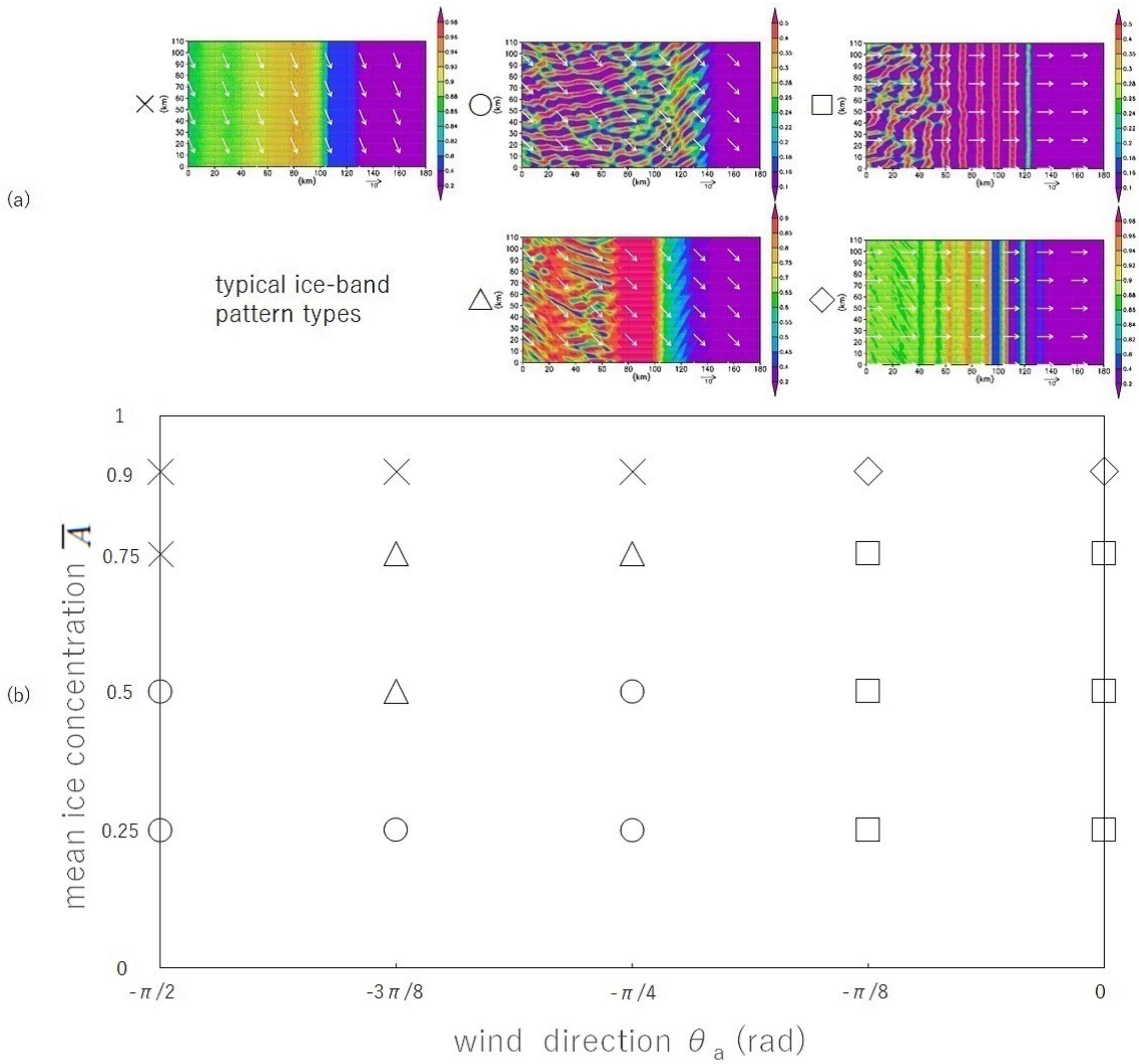

Figure 19: Ice-band pattern distribution with respect to wind direction and ice concentration. (a) Typical types of ice-band pattern. × denotes a pattern without band formation. ○ denotes a pattern dominated by the effect of initial random ice concentration. △ denotes a pattern representing band formation due to initial random ice concentration in the interior ice field along with an effect of ice-edge without band formation. □ denotes a pattern representing band formation due to both the effect of ice edge and the effect of the initial random ice concentration. ◇ denotes a pattern dominated by the effect of ice edge with band formation. White arrows in the patterns denote wind vectors. (b) Ice-band pattern type distribution with respect to wind direction θ_a and ice concentration $\overline{A}$.

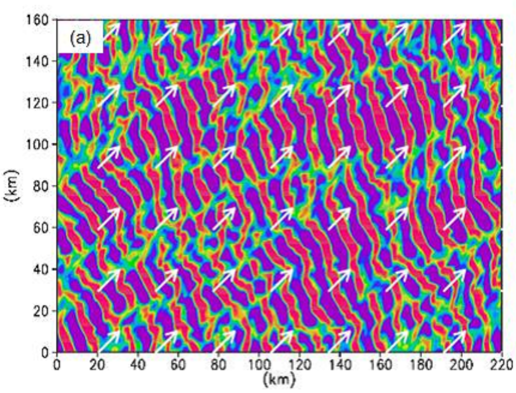

Figure 20: Effect of ice thickness on the ice-band pattern formation. Ice thickness of (a) 0.1 m and (b) 1.0 m. Results on day 7 are shown. The color shade denotes the sea-ice concentration.

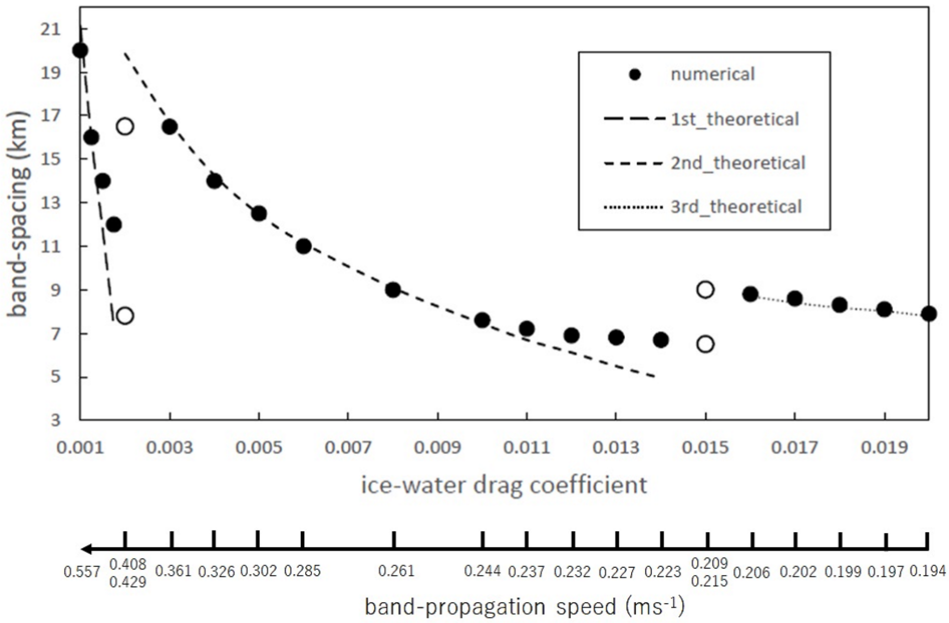

Figure 21: Relationship between ice-water drag coefficient C_{Diw} and band spacing λ. ● denotes numerical results. ○ denotes cases that give two numerical values for a single drag coefficient. Three curves in this figure denote theoretical results of 1st, 2nd, and 3rd modes, respectively, evaluated by the band propagation speed with varying C_{Diw}.

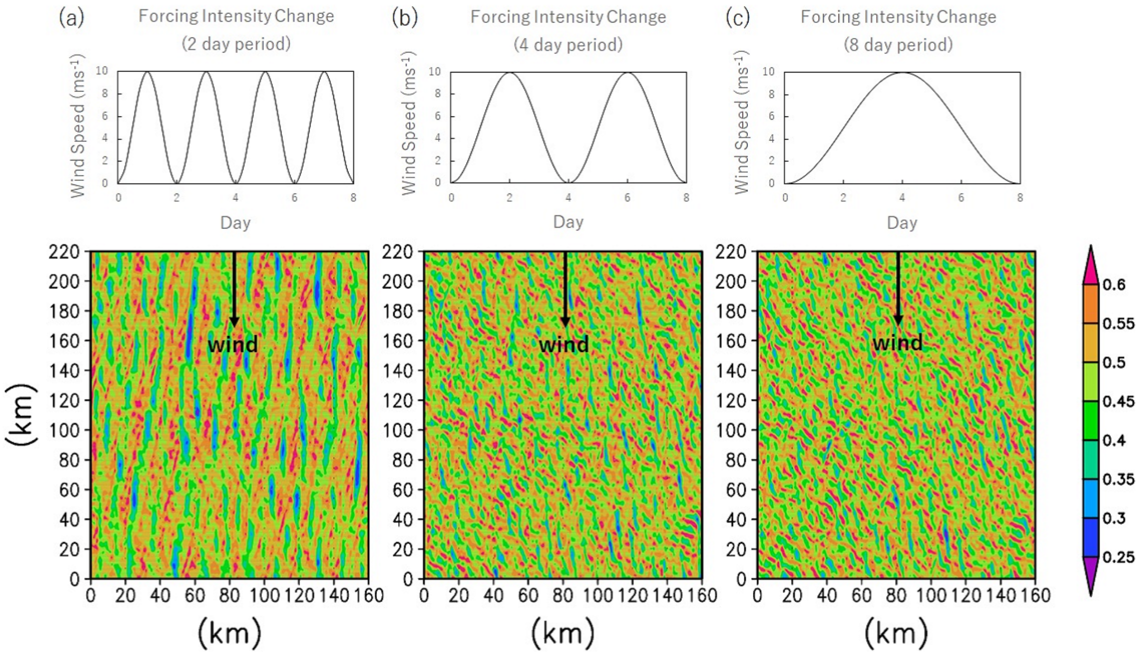

Figure 22: Experiments with variable wind intensities. The wind intensity varied with (a) 2-day, (b) 4-day, and (c) 8-day periods. The upper panels display the wind intensity with time, while the lower panels display numerical results on day 7. The color shade in the lower panels denotes the sea-ice concentration

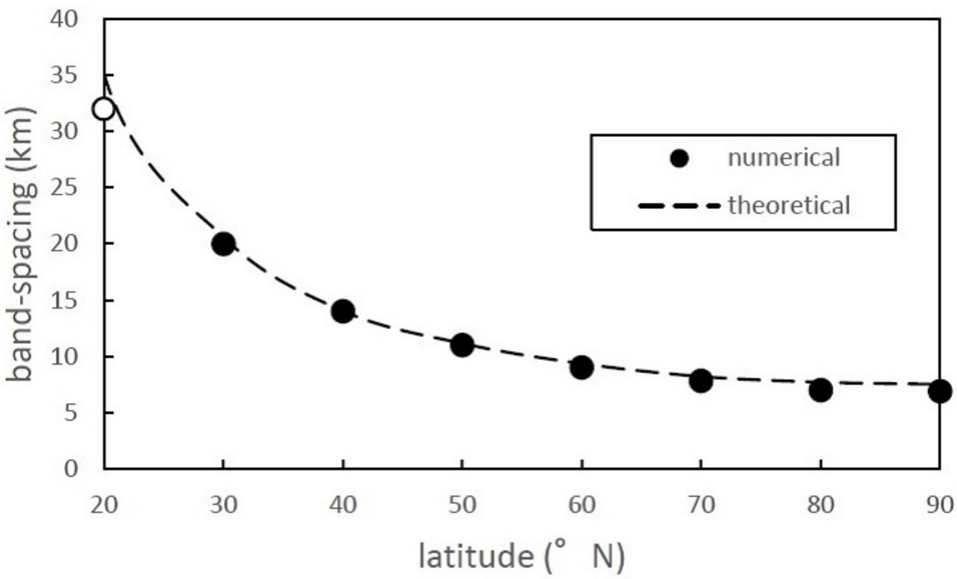

Figure 23: Relationship between latitude (Coriolis parameter) and band spacing. ● denote the numerical results. Dashed curve indicates the theoretical results.

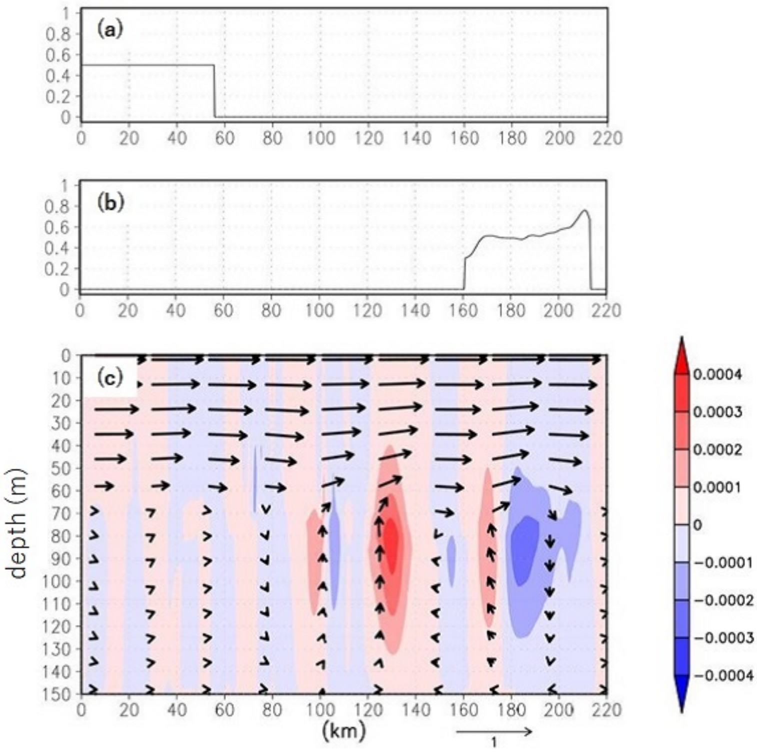

Figure 24: Non-rotational experiment. (a) Initial sea-ice concentration. (b) Sea-ice concentration 4 days after the initial state. (c) Vertical section of the velocity field. The vector unit is ms^{-1}. The vertical velocity is multiplied by 1000 to draw the vectors. The color shade denotes the vertical velocity.